Acta Geotechnica manuscript No.
(will be inserted by the editor)

A Thermo-Mechanical Damage Model for Rock Stiffness during Anisotropic Crack Opening and Closure

Cheng Zhu · Chloé Arson

Received: date / Accepted: date

Abstract A thermodynamic framework is proposed to couple the effect of mechanical stress and temperature on crack opening and closure in rocks. The model is based on Continuum Damage Mechanics, with damage defined as the second-order crack density tensor. The free energy of the damaged rock is expressed as a function of deformation, temperature and damage. The damage criterion captures mode I crack propagation, the reduction of toughness due to heating, and the increase of energy release rate with cumulated damage. Crack closure is modeled through unilateral effects produced on rock stiffness. The model was calibrated and verified against published experimental data. Thermo-mechanical crack opening (resp. closure) was studied by simulating a triaxial compression test (resp. uniaxial extension test) including a thermal loading phase. The degradation of stiffness due to tensile stress and recovery of stiffness induced by both mechanical and thermo-mechanical unilateral effects are well captured. The thermo-mechanical energy release rate increases with thermal dilation, and also decreases with ambient temperature. It was observed that there is a temperature threshold, below which the rock behaves elastically. A parametric study also showed that the model can capture hardening and softening during thermo-mechanical closure (for specific sets of parameters). These numerical observations may guide the choice of rock material used in geotechnical design, especially for nuclear waste disposals or compressed air storage facilities.

Keywords Rock Constitutive Behavior · Continuum Damage Mechanics · Thermo-Mechanical Couplings · Unilateral effect · Damage-Induced Anisotropy

C. Zhu · C. Arson
School of Civil and Environmental Engineering,
Georgia Institute of Technology, Atlanta, GA, USA
E-mail: chengzhu@gatech.edu, chloe.arson@ce.gatech.edu

1 Introduction

Most of the research on rock mechanics is motivated by societal needs such as energy production, energy storage, and waste disposal. Safety and sustainability are key issues in the design of the underground geotechnical facilities and the foundations of structures needed to sustain the fuel cycle. Design is based on the careful use of constitutive models formulated according to theoretical requirements and/or experimental observations [7, 31]. In particular, crack initiation and propagation is a critical concern [27, 59]. In addition to mechanical damage, nuclear waste repositories and geothermal systems are exposed to significant temperature gradients over time. Radioactive packages disposed in the repositories release heat with an exponent decay of power, responsible for a long-term increase in the temperature of the surrounding rock mass [56]. The dramatic changes in temperature associated with geothermal reservoir exploitation also affect rock properties [67]. This raises the necessity to formulate reliable thermo-mechanical damage models for rocks.

Thermo-mechanical couplings are of primary importance in many geomaterials. In clay for instance, temperature changes affect stiffness and deformation mostly through thermo-hydro-mechanical couplings: temperature affects the density and viscosity free and adsorbed water [50]. It is well-known that normally consolidated and overconsolidated clays exhibit different thermoplastic behaviors under thermo - mechanical stress paths [37]. The critical state theory was combined with thermo-plastic soil behavior models [38] in order to predict macroscopic effects of temperature changes. Long-term thermo-mechanical behavior of in-situ clay was investigated through a chemo-thermo-plastic model [39]. Thorough experimental studies enabled relating soil physical properties (e.g., friction angle, permeability) to soil macroscopic thermo - mechanical properties (e.g., elastic moduli) [9, 49]. The structure of the porous space in the medium is a sig-

nificant factor that has been accounted for in many thermo-hydro-mechanical coupled models. Description of heat transfer in the porous space adds to the difficulty of such formulations: heat is exchanged by convection and conduction, while the viscosity of pore fluids is temperature-dependent [73]. In addition, evaporation and condensation may affect the transport of heat [25].

Thermo-mechanical stress gradients can originate various micro-structure changes, leading to various material property changes. Chain force models are appropriate for granular materials [16]. For rocks, fracture mechanics provides a powerful theoretical framework when the crack propagation mode is known [48]. In fact, relating microscopic processes (such as void nucleation, mode I crack opening, and linkage of shear cracks) to macroscopic rock properties (stiffness, permeability) is a challenging issue [58]. Coupled processes impacting both physical and mechanical properties were studied experimentally, both in the laboratory and in situ [20]. Of particular interest are the observations made to relate microstructure and physical properties [26, 47], damage and density [87], porosity and permeability [24, 57, 83], crack density and electrical conductivity [20], damage and wave velocity [13, 71]. Studies were also dedicated to the response of rock under frost action [61]. Large scale in-situ tests were mainly carried out to monitor the evolution of thermo-mechanical damage [51] and study the variation of physical properties like permeability [44, 72] under thermo-mechanical effects. It is generally observed that mechanical properties of rocks such as elastic moduli [30, 82], compressive strength [43, 65, 84] or tensile strength [34], as well as cohesion and friction angle [56], and fracture toughness [68] decrease when temperature increases. The trends expected for specific rock types are summarized in [32].

In Continuum Damage Mechanics (CDM), the strain energy loss due to crack propagation is used to compute damaged stiffness and deformation. This approach is purely energetic and does not require a geometric description of the crack pattern. The second-order crack density tensor [45] is particularly well-suited to evaluate damaged elastic properties of a solid with non-interacting cracks. Closure of tensile cracks allows recovery of compressive strength and not tensile strength. These so-called "unilateral effects" were studied in detail by Mazars et al. for concrete [66]. A way of formulating the unilateral condition for active/passive damage was proposed in [12]. The anisotropic mechanical model of crack closure was later extended to account for frictional sliding at crack faces [28]. Various models were proposed to predict thermo-mechanical damage, but most of these models partially uncouple thermal and mechanical effects, so that damage does not truly depend on temperature variations, but rather on thermo-mechanical stress [88]. In salt rock, damage is associated with a crack-induced volumetric deformation, captured by a "dilatancy boundary" [35, 40]. This class of models (see also [14]) do not capture stiffness changes and could not predict damage-induced anisotropy in a sedimentary rock.

In this study, a thermodynamic framework based on CDM is proposed to model the effects of thermo-mechanical crack opening and closure on rock stiffness. Section 2 presents a state-of-the-art of laboratory observations and thermodynamic models for thermo-mechanical damage in rock. The theoretical framework of the proposed constitutive model is explained in Section 3, which puts the emphasis on the assumptions made to express the damage-driving force. The model was calibrated and verified against published experimental data, and the results are presented in Section 4. Section 5 presents simulations of different stress paths, including crack opening and closure under both mechanical and thermo-mechanical stresses. The same stress paths were then simulated for different types of rocks, and the results are discussed in Section 6.

2 State of the art: thermo-mechanical damage in rock

2.1 Experimental assessment of thermo-mechanical damage in rock

Rock thermo-mechanical behavior was investigated with a variety of stress paths, both at laboratory scale and field scale. Different types of mechanical loading conditions were considered, including monotonic/cyclic, uniaxial/triaxial, short term/long term, and drained/undrained. Table 1 provides the strength and Young's modulus of rocks of interest for geological storage purposes. Rock samples were tested in the laboratory under different thermo - mechanical stress paths, mainly: (1) a temperature-controlled mechanical loading, or (2) a heating phase followed by a mechanical loading, or (3) a heating phase followed by a relaxation period (until the temperature of the sample reached room temperature) followed by a mechanical loading. Most of the experimental results reported in the literature focus on rock compressive strength. Temperature changes were limited to less than $1000\,^{\circ}\mathrm{C}$ to prevent any chemical change in rock minerals. Most often, rocks were subjected to a heating phase. To the authors' best knowledge, only granite and tuff were studied upon cooling. Rock stiffness tends to increase (resp. decrease) upon cooling (resp. heating). Granite has the highest compressive strength among all the rocks tested. In gabbro, there exists a critical temperature above which drastic change in mechanical properties occur [47]. Confined salt rock is subject to complex time-dependent microscopic processes, such as dislocation, glide, and cross-slip. At the bulk scale, coupled processes make it challenging to discriminate visco-plastic (dislocation-induced) deformation and damage (crack-induced) deformation. Overall, creep processes in salt

rock result in much larger deformation at failure compared to other types of rock [82].

2.2 Thermo-mechanical damage models for rock: Continuum Damage Mechanics approaches

Micro-mechanical damage models [22, 54] assume that the rock Representative Element Volume (REV) is populated with a given distribution of cracks characterized by a specific shape (usually, spherical, penny-shaped or ellipsoidal cracks). Assumptions on the shape and density of cracks allow to express explicitly the strain concentration tensor, and further, to derive the theoretical expression of the Helmholtz free energy of the rock solid skeleton. For dilute distributions of cracks, the self-consistent method proved to provide an efficient scheme to model the loss of stored elastic deformation energy induced by cracking. If microscopic cracks open in pure mode I, i.e. if the crack displacement vector is normal to the crack planes, the only damage variable needed to express the dissipation of energy associated to the degradation of elastic moduli is the second-order crack density tensor, defined by Kachanov [45] as:

$$\mathbf{\Omega} = \sum_{k=1}^{N} d_k \mathbf{n}_k \otimes \mathbf{n}_k \tag{1}$$

In which the REV is assumed to contain N planar cracks with a normal direction $\mathbf{n}_k$ and a volumetric fraction d_k. Mixed crack propagation modes (inducing a non-zero tangential displacement at crack faces) would require higher damage tensors - at least of order four [8, 11, 28]. Increasing the order of the damage tensor generally improves the compliance of the model to symmetry properties required for the elasticity tensor [63]. In fact, the second-order density tensor emerging from micro-mechanical analyses is a particular form of Oda's fabric tensor, commonly used in structural geology [69]:

$$\mathbf{F} = \frac{\pi}{4} \frac{N}{V_{REV}} \int_0^{\infty} \int_{\Omega} r^3 E(r, \mathbf{n}) \, \mathbf{n} \otimes \mathbf{n} \, d\mathbf{n} dr \tag{2}$$

In which $E(r, \mathbf{n})$ is the mathematical expectancy of the presence of a crack of radius r and normal direction $\mathbf{n}$ in a REV of size V_{REV}. For a given crack density and with given probability density functions of crack shapes and orientations, a direct relationship can be established between fabric tensors and rock elasticity tensor [19, 63]. The key issue is to choose relevant microstructure descriptors [52, 62] and associated probability density functions.

So-called phenomenological models are based on energy postulates (i.e. assumptions need to be made on the expression of the free energy and dissipation of the REV) rather than hypotheses on micro-structure geometry. Such formulations often resort to the concept of effective stress, which stands for the stress developed in the fictive undamaged counterpart of the system [6]. The principle of equivalent elastic energy or the principle of equivalent elastic deformation [53] then makes it possible to compute the damaged stiffness tensor, provided that the expression of the free energy of the solid skeleton of the rock is given (i.e. postulated). The key point consists in defining a damage operator to express the effective stress as a function of damage and of the stress applied at the boundaries (far-field stress), so as to satisfy the symmetry and positivity requirements for the elasticity tensor [18]. Three postulates are needed to close the damage model formulation: the expression of the free energy Ψ (dependent on the expression of the damage operator), the expression of a damage criterion (often noted f_d), and the expression of a damage potential (often noted g_d). Note that in most CDM models used for rock so far, damage flow rule was assumed to be associate, i.e. the damage criterion was used as a damage potential [2, 3, 74]. Moreover, many damage models for rock allowed the prediction of residual strains (i.e. deformation remaining in the sample after a bare stress relaxation), without resorting to any additional plastic potential [1, 28]. Even so, two flow rules are needed to close the model formulation [86]: the rate of inelastic deformation and the rate of damage (affecting the stiffness tensor). Table 2 summarizes the postulates made in phenomenological thermo-mechanical damage models proposed for rock. Most models are based on a purely mechanical damage evolution law, which implies that temperature can only affect damage if the tensile stress induced by heating exceeds the threshold of mechanical tensile strain necessary to open cracks. In practice, this means that most models are based on the expression of a damaged stiffness tensor, introduced in a thermo-elastic stress/strain relationship.

3 A phenomenological model to predict the influence of thermo-mechanical crack opening and closure on rock stiffness

3.1 Outline of the modeling approach

The modeling approach adopted herein is illustrated in Fig. 1. The free energy is sought in the form of a function of state variables (in this thermo-mechanical study: deformation ε and temperature T) and internal (dissipation) variables (in the present case: the damage tensor $\mathbf{\Omega}$). The damage flow rule is assumed to be associate, which implies that the damage potential is equal to the damage criterion. The latter shall depend on damage and on the damage-driving force that is work-conjugate to damage. The damage-driving force is sought in the form of a function of both mechanical stress and temperature, in order to predict crack propagation under thermo-mechanical stress gradients. Crack closure can be accounted for by introducing a unilateral condition in the

Table 1 State of the art: experimental assessment of thermo-mechanical damage in rock

Material	Experimental test	T (°C)	Peak stress σ_P (MPa)	Strain at peak stress ε_P	Stiffness (GPa) (high T - low T)	References
Limestone	uniaxial compression test without cooling	25 ∼ 800	25 ∼ 110	0.005 ∼ 0.013	3.2 ∼ 17.8 (E)	[85]
	uniaxial compression test after cooling	20 ∼ 250	43.2 ∼ 46.4	0.0023 ∼ 0.0029	23.7 ∼ 25 (E)	[57]
Salt rock	triaxial compression test without cooling	23 ∼ 200	15 ∼ 65	0.02 ∼ 0.35	29.6 ∼ 36.5 (E)	[82]
	uniaxial compression test without cooling	20 ∼ 180	10 ∼ 22	0.005 - 0.018	1.14 ∼ 2.15 (E_t)	[56]
Gabbro	uniaxial compression test after cooling	25 ∼ 1000	35 ∼ 230	0.0023 ∼ 0.006	2.5 ∼ 85 (E)	[47]
Breccia	uniaxial compression test after cooling	20 ∼ 800	92.4 ∼ 130.3	0.0034 ∼ 0.0045 (high T - low T)	11.8 ∼ 30.3 (E)	[89]
Granite	triaxial compression test without cooling	20 ∼ 700	600 ∼ 1150	0.015 ∼ 0.025	32 ∼ 60 (E)	[84]
	uniaxial compression test without cooling	20 ∼ 600	150 ∼ 260	0.007 ∼ 0.014	20 ∼ 50 (E_t)	[34]
	uniaxial tension test without cooling	20 ∼ 600	1 ∼ 9	0.0002 ∼ 0.0006	5 ∼ 20 (E)	[34]
	uniaxial compression test and radial compression test under thermal hysteresis without restoring to room temperature	-160 ∼ 100	σ_c heat: 155 ∼ 195 cool: 180 ∼ 220 σ_t heat: 8 ∼ 9.5 cool: 8.5 ∼ 14	heat: 0.00015 ∼ 0.0008 cool: -0.0018 ∼ -0.0001 (ε_τ)	heat: 46 ∼ 54 cool: 40 ∼ 50 (E_t)	[42]
	uniaxial compression test after cooling	20 ∼ 800	105.5 ∼ 152.9	0.0026 ∼ 0.0099	15.9 ∼ 32.4 (E)	[89]
Andesite	uniaxial compression test without cooling	23 ∼ 200	100 ∼ 117	0.0062 ∼ 0.0093	16 ∼ 21 (E)	[43]
Mudstone	uniaxial compression test without cooling	25 ∼ 800	25 ∼ 275	0.0045 ∼ 0.013	6.6 ∼ 24.7 (E)	[60]
Tuff	uniaxial compression test and radial compression test under thermal hysteresis without restoring to room temperature	-160 ∼ 100	σ_c heat: 10 ∼ 15 cool: 22 ∼ 30 σ_t heat: 1.5 ∼ 2.3 cool: 2 ∼ 4	heat: 0.0001 ∼ 0.0007 cool: -0.0016 ∼ -0.0001 (ε_τ)	heat: 3.2 ∼ 4 cool: 3.5 ∼ 4.6 (E_t)	[42]
	uniaxial compression test after cooling	20 ∼ 800	101.6 ∼ 147.7	0.0043 ∼ 0.0069	19.9 ∼ 30.7 (E)	[89]
Marble	uniaxial compression test after cooling	20 ∼ 600	57 ∼ 131	0.0087 ∼ 0.0123	9.18 ∼ 16.8 (E)	[75]

Notations: E = elastic modulus; E_t = tangent modulus; σ_c = compressive strength; σ_t = tensile strength; T = temperature; ε_τ = thermal strain

expression of the damaged elastic stiffness used in the free energy [11]. Energy is dissipated due to both mechanical and thermal effects, therefore the Inequality of Clausius-Duhem (ICD) writes:

$$(\sigma : \dot{\varepsilon} - \dot{\tau} S - \dot{\Psi}_S) + (-\frac{\mathbf{q}}{\tau} \cdot \nabla \tau) \geq 0 \tag{3}$$

where Ψ_S and S are the free energy and the entropy of the rock solid skeleton, respectively. $\mathbf{q}$ is the heat flow, and τ represents the variation of temperature compared to a given reference state. Mechanical dissipation (first term of Eq. 3) and thermal dissipation (second term of Eq. 3) are usually considered both positive (*stricto sensu*, these two requirements are sufficient but not necessary to satisfy Eq. 3). Constitutive equations (such as the stress/strain relationship) are obtained by introducing the postulated expressions of the free energy and the damage associate flow rule in the ICD.

3.2 Free energy of the damaged rock skeleton

The damage variable ($\mathbf{\Omega}$) used in the proposed model is defined as the second-order crack density tensor (Eq. 1), projected in its principal base. Assuming that rock has a linear thermo-elastic behavior in the absence of damage, the free

Table 2 State of the art: phenomenological models of thermo-mechanical rock damage

Main governing equations	"Stress" paths simulated	Phenomena observed	References
$\Psi = \Psi^e(\varepsilon_e, T, \Omega) + \Psi^p(\gamma^p, T, \Omega) + \Psi^{vp}(\gamma^{vp}, T, \Omega)$, $f^p(\sigma, \eta) = q - g(\theta)\eta^p(T, \gamma^p, \Omega)R_c(C_s + \frac{p}{R_c})^m$, $g^p = q - (\eta^p - \beta^p)(p + C_s R_c)$, $f^\omega(Y^\omega, \Omega) = Y^\omega - r(\Omega) \leq 0$	(1) triaxial compression tests (different confining stress, different T); (2) creep tests (different stresses, different T)	temperature variable is introduced in hardening function; capture both long-term and short-term deformation behavior under thermal effect	[88]
$\Psi = \Psi_e - g_M \Omega : \varepsilon_M - \frac{g_S}{3}\Omega : \delta\varepsilon_{Sv} - \frac{g_T}{3}\Omega : \delta\varepsilon_T$, $\Psi_e = \frac{1}{2}\varepsilon_M : D_e(\Omega) : \varepsilon_M + \frac{1}{2}\varepsilon_{Sv}\beta_s(\Omega)\varepsilon_{Sv} + \frac{1}{2}\varepsilon_T\beta_T(\Omega)\varepsilon_T$, $f_d(Y_{d1}{}^+, \Omega) = \sqrt{\frac{1}{2}Y_{d1}{}^+ : Y_{d1}{}^+} - (C_0 + C_1\Omega)$	(1) isothermal drained and undrained triaxial compression tests; (2) study the behavior of an unsaturated massif hosting a heating source	damage influences heat transfer isotropically; damage increases with higher damage rigidities; water permeability grows with damage and with the internal length parameter	[2]
$\Psi = \frac{1}{2}\varepsilon : E(d, g) : \varepsilon - Tn(d, g) : \varepsilon - \frac{1}{2}c\frac{T^2}{T_0}$, $f_d = \bar{\varepsilon} - k(d, T)$, $f_g = T - \bar{k}(g, T)$	heating without loading, and then the temperature is kept constant while load is applied	specific heat depends on damage; positive dissipation when thermal energy is in logarithmic form	[76]
$\Psi = W(\varepsilon_e^i, \kappa, d^+, d^-) + V(T) + L(T, \xi) + H(\xi)$, $W = (1 - d^+)W_e^+(\varepsilon_e^i, \kappa) + (1 - d^-)W_e^-(\varepsilon_e^i, \kappa)$, $\hat{f}^\pm = \sqrt{\bar{\sigma}^\pm : C^\pm : \bar{\sigma}} - f_e^\pm r^\pm$, $\varepsilon_T = \alpha_T(T - T_0)$	(1) short term test with isothermal or adiabatic conditions considered; (2) long term test with monotonic or cyclic loadings	both the elastic moduli and the strength depend on the hardening; strain-drivien model allows its possibility for large-scale computation	[10]
$\Psi = \varepsilon_c(J_s) + \Psi_T(J_s, T) + \frac{G(J_s,T)(\alpha_1 - 3)}{2\rho_{s0}}$, $Y_f = Y_c(c_m + \frac{c_n p}{Y_c} - \frac{c_n Y_f}{3Y_c})^z$, $Y(\phi, p, \theta, \Omega, \delta_h, T) = Y_{\text{TXC}}(p)F_{\text{Lode}}(\theta)F_{\text{therm}}(J_s, T)$, $F_{\text{therm}(J_s,T)=G(J_s,T)/G(J_s,T=0)}$	(1) uniaxial/triaxial compression to a single joint set and randomly jointed volumes; (2) wave propagation induced by spherical explosions	use a 3D contact algorithm to model block interaction; account for rocks with various rock quality and porosity; effective properties of jointed rocks is available numerically in explicit calculations	[80]
$\Psi = \Psi(\varepsilon - \varepsilon^p, T) = e - sT$, $f^p = \sqrt{J_2} + \alpha I_1 - k_m$, $g^p = \sqrt{J_2} + \beta I_1$, $\rho c\dot{T} = -\nabla q_h + (\sigma : \dot{\varepsilon}^p - \alpha_T T\delta : C : \dot{\varepsilon}^e)$	(1) excavation of test tunnel and deposition holes under isothermal condition; (2) heating of rock pillar for one hundred days in total	elastic and elastoplastic models cannot accurately describe the failure process; heating increases the tangential stress on the pillar wall	[15]

Ψ = Helmholtz's free energy
Ψ^e = degraded elastic free energy
Ψ^p, Ψ^{vp} = plastic, visco-plastic strain energy
e = specific internal energy
V, Ψ_T = thermal part of free energy
W = mechanical free energy
L = thermomechanical part of free energy
H = chemical part of free energy
ε_c = volume-dependent potential
Y^ω, Y_d = damage conjugate force
R_c, Y_c = unconfined compressive strength
Y_f = failure strength
Ω = damage variable
d = mechanical damage parameter
g = thermal damage parameter
p = mean stress
q = deviatoric stress
θ = Lode angle
m = curvature of yield surface
n = thermo-elastic coupling tensor
K_w = permeability
d^+, d^- = damage indices

g_M, g_S, g_T = crack-related rigidity
D_e, β_s, β_T = damaged stiffness
r = damage energy release threshold
β^p = transition point
η^p = instantaneous plastic hardening
$\bar{\sigma}, \sigma$ = stress tensor
ε_e = elastic strain
ε_M = mechanical strain
ε_{sv} = capillary volumetric strain
ε_T = thermal volumetric strain
$\bar{\varepsilon}$ = non-local equivalent strain
α_T = thermal expansion coefficient
$f^\pm, f^p, f^{vp}$ = yield criterion
γ^p, γ^{vp} = hardening variable
g^p, g^{vp} = plastic potential
c = specific heat capacity
C = tangential modulus tensor
C_0 = initial damage-stress rate
C_1 = damage increase rate
$C^\pm$ = tensile/compressive metric tensor
c_m, c_n, z = material parameter
C_s = coefficient of material cohesion

k_m = material property
q_h = heat conduction
J_2 = deviatoric stress invariant
I_1 = principal stress invariant
α, β = experimental coefficient
ρ = density
ϕ = porosity
Y_{TXC} = triaxial compression yield strength
α_1 = invariant of symmetric unimodular tensor
$k, \bar{k}$ = hardening-softening parameter
κ = aging degree
$r^\pm$ = damage threshold
$f_e^\pm$ = elastic limit in uniaxial test
G = shear modulus
ξ = hydration degree
T = absolute temperature
T_0 = reference temperature
s = entropy
F_{therm} = thermal softening term
F_{lode} = Lode angle function
ε^{id} = irreversible strain
J_s = average dilatation of the solid

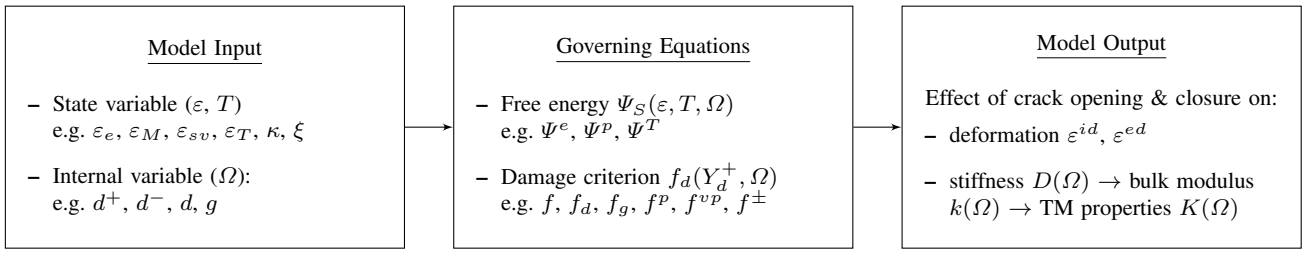

Fig. 1 Modeling Approach: the proposed model is formulated with two state variables (deformation and temperature), and one dissipation variable (damage); two postulates are needed: the expression of the free energy of the rock solid skeleton, and the damage criterion (also used as a damage potential); the properties and variables predicted by the model are deformation, stiffness and the thermo-mechanical modulus $K(\Omega)$ (depending on stiffness); other possible choices for the model formulation are indicated to compare the present model to the models found in the literature (Table 2).

energy of the rock solid skeleton (Ψ_S) is sought in the form of a polynomial of order two in deformation. The polynomial is assumed to be linear in damage in order to avoid the non-linearities involved in having the energy release rate (work-conjugate to damage) depend on damage:

$$\Psi_S(\boldsymbol{\varepsilon}, \tau, \boldsymbol{\Omega}) = \frac{1}{2}\boldsymbol{\varepsilon}^{\boldsymbol{E}} : \mathbf{D}(\boldsymbol{\Omega}) : \boldsymbol{\varepsilon}^{\boldsymbol{E}} + g\boldsymbol{\Omega} : \boldsymbol{\varepsilon} - \frac{1}{2\tau_0}C(\boldsymbol{\Omega})\tau^2 - \tau\mathbf{K}(\boldsymbol{\Omega}) : \boldsymbol{\varepsilon}^{\boldsymbol{E}} \quad (4)$$

In which $\mathbf{D}(\boldsymbol{\Omega})$ is the damaged stiffness tensor. The term $g\boldsymbol{\Omega} : \boldsymbol{\varepsilon}$ represents the energy that needs to be released to close residual cracks (i.e., cracks that remain open after releasing a tensile loading). The two last terms of the free energy ($-\frac{1}{2\tau_0}C(\boldsymbol{\Omega})\tau^2 - \tau\mathbf{K}(\boldsymbol{\Omega}) : \boldsymbol{\varepsilon}^{\boldsymbol{E}}$) are the classical linear thermo-elastic energy potentials. τ_0 is the initial temperature, τ is the temperature change, $C(\boldsymbol{\Omega})$ is the damaged heat capacity. The coefficients of the diagonal tensor $\mathbf{K}(\boldsymbol{\Omega})$ are equal to the product of the damaged bulk modulus $k(\boldsymbol{\Omega})$ by the thermal expansion coefficient of the solid skeleton (α_T). Note that the thermal expansion coefficient α_T is assumed to remain constant, while the bulk modulus $k(\boldsymbol{\Omega})$ depends on damage. This is because in the undamaged part of the bulk (i.e. outside the cracks), solid thermal properties are unchanged. The mechanical part of the proposed model is based on Halm & Dragon's model [28], which proved to perform well in predicting brittle rock behavior. However, the model proposed herein is different not only because thermo-mechanical couplings are introduced, but also because total deformation ($\boldsymbol{\varepsilon}$) was replaced by elastic deformation ($\boldsymbol{\varepsilon}^{\boldsymbol{E}}$) in the damaged elastic potential (first part of Eq. 4). This substitution of deformation variable has important implications on the phenomenological definition of stress in the model, as will be explained later in this subsection. The damaged elastic deformation energy is written:

$$\frac{1}{2}\boldsymbol{\varepsilon}^{\boldsymbol{E}} : \mathbf{D}(\boldsymbol{\Omega}) : \boldsymbol{\varepsilon}^{\boldsymbol{E}} = \frac{1}{2}\lambda(tr\boldsymbol{\varepsilon}^{\boldsymbol{E}})^2 + \mu\, tr(\boldsymbol{\varepsilon}^{\boldsymbol{E}} \cdot \boldsymbol{\varepsilon}^{\boldsymbol{E}}) + \alpha\, tr\boldsymbol{\varepsilon}^{\boldsymbol{E}}\, tr(\boldsymbol{\varepsilon}^{\boldsymbol{E}} \cdot \boldsymbol{\Omega}) + 2\beta\, tr(\boldsymbol{\varepsilon}^{\boldsymbol{E}} \cdot \boldsymbol{\varepsilon}^{\boldsymbol{E}} \cdot \boldsymbol{\Omega}) \quad (5)$$

The damage-induced irreversible strain $\boldsymbol{\varepsilon}^{id}$ is defined as:

$$\boldsymbol{\varepsilon}^{id} = \boldsymbol{\varepsilon} - \boldsymbol{\varepsilon}^{E} \quad (6)$$

In Eq. 5 above, λ and μ are Lam*é* coefficients (for the undamaged material). α, and β are damaged material parameters. For convenience, a condensed notation is adopted:

$$\Psi_S(\boldsymbol{\varepsilon}, \tau, \boldsymbol{\Omega}) = \frac{1}{2}\boldsymbol{\varepsilon}^{\boldsymbol{E}} : \mathbf{D}_T(\tau, \boldsymbol{\Omega}) : \boldsymbol{\varepsilon}^{\boldsymbol{E}} - \frac{1}{2\tau_0}C(\boldsymbol{\Omega})\tau^2 + g\boldsymbol{\Omega} : \boldsymbol{\varepsilon} \quad (7)$$

In which $\mathbf{D}_T$ is the damaged thermo-elastic tensor. The proposed thermo-mechanical damage model is formulated with a minimum number of postulated functionals. Irreversible strain $\boldsymbol{\varepsilon}^{id}$ is assumed to be entirely attributed to the damage parameter $\boldsymbol{\Omega}$, and accordingly, only one "yield" criterion is introduced in the model. The damage evolution law is obtained by applying a pseudo-associate flow rule (more details on the definition of the damage driving force are provided in the next subsection). A rigorous thermodynamic formulation would require deriving the evolution law of $\boldsymbol{\varepsilon}^{id}$ from Legendre transformations of dissipation potentials, as explained in [17]. In fact a long-standing debate exists in thermodynamics of irreversible processes regarding the nature of the variables that shall be employed in energy potentials. Introducing non-plastic, purely damage-induced irreversible deformation raises thermodynamic consistency issues, some of which are explained in [21, 36, 41, 46, 81], to cite only a few references. Future theoretical work will be undertaken by the authors and their collaborators to derive a closed-form formulation from a single damage potential for both damage and damage-induced irreversible deformation, within a thermodynamically consistent framework.

The work presented in this paper focuses on constitutive modeling, and provides a unified framework to predict damage in rock subjected to crack opening and closure under thermo-mechanical stresses. For the sake of this study, the proposed model is based on state-of-the-art Continuum Damage Mechanics. Stress is defined as the work-conjugate of total deformation. The thermodynamic force conjugate to elastic strain $\boldsymbol{\varepsilon}^{\boldsymbol{E}}$ is viewed as an equivalent stress $\boldsymbol{\sigma}^{eq}$, as defined in [2, 78]:

$$\boldsymbol{\sigma} = \boldsymbol{\sigma}^{eq} + \boldsymbol{\sigma}_R = \boldsymbol{\sigma}^{eq} + g\boldsymbol{\Omega} \quad (8)$$

In which $\boldsymbol{\sigma}_R = g\boldsymbol{\Omega}$ is the stress needed to close the cracks that remain open after releasing a tensile loading. Fig. 2 explains the decompositions of stress and strain assumed in the model, which lead to:

$$\boldsymbol{\sigma} = \mathbf{D}_T(\tau, \boldsymbol{\Omega}) : \boldsymbol{\varepsilon} \; = \; \mathbf{D}_T(\tau, \boldsymbol{\Omega}) : \boldsymbol{\varepsilon}^E \; + \mathbf{D}_T(\tau, \boldsymbol{\Omega}) : \boldsymbol{\varepsilon}^{id} \tag{9}$$

Conveniently, the constitutive assumptions made allow obtaining the evolution of irreversible strain as follows:

$$\boldsymbol{\varepsilon}^{id} \; = \; g\mathbf{D}_T(\tau, \boldsymbol{\Omega})^{-1} : \boldsymbol{\Omega} \tag{10}$$

Conjugation relationships also provide the energy release rate (also called damage-driving force), which is further decomposed into two parts:

$$\mathbf{Y} = -\frac{\partial \boldsymbol{\Psi}_{\mathbf{S}}(\boldsymbol{\varepsilon}, \tau, \boldsymbol{\Omega})}{\partial \boldsymbol{\Omega}} = \mathbf{Y_1} + \mathbf{Y_2} \tag{11a}$$

$$\mathbf{Y_1} = -g\boldsymbol{\varepsilon} - \alpha(tr\boldsymbol{\varepsilon}^E)\boldsymbol{\varepsilon}^E - 2\beta(\boldsymbol{\varepsilon}^E \cdot \boldsymbol{\varepsilon}^E) \tag{11b}$$

$$\mathbf{Y_2} = \frac{1}{2\tau_0}\frac{\partial \mathbf{C}(\boldsymbol{\Omega})}{\partial \boldsymbol{\Omega}}\tau^2 + \tau\frac{\partial \mathbf{K}(\boldsymbol{\Omega})}{\partial \boldsymbol{\Omega}} : \boldsymbol{\varepsilon}^E \tag{11c}$$

Stress evolution writes:

$$d\boldsymbol{\sigma} = \mathbf{D}(\boldsymbol{\Omega}) : d\boldsymbol{\varepsilon}^{\boldsymbol{E}} + (\frac{\partial \mathbf{D}(\boldsymbol{\Omega})}{\partial \boldsymbol{\Omega}} : \boldsymbol{\varepsilon}^{\boldsymbol{E}}) : d\boldsymbol{\Omega} + gd\boldsymbol{\Omega} \\ -\mathbf{K}(\boldsymbol{\Omega})d\tau - (\frac{\partial \mathbf{K}(\boldsymbol{\Omega})}{\partial \boldsymbol{\Omega}}d\boldsymbol{\Omega})\tau \tag{12}$$

The total deformation tensor is split into three components [1], as shown in Fig. 2:

$$\boldsymbol{\varepsilon} = \boldsymbol{\varepsilon}^{\boldsymbol{el}} + \boldsymbol{\varepsilon}^{\boldsymbol{ed}} + \boldsymbol{\varepsilon}^{\boldsymbol{id}} = \boldsymbol{\varepsilon}^{\boldsymbol{E}} + \boldsymbol{\varepsilon}^{\boldsymbol{id}} \tag{13}$$

In which $\boldsymbol{\varepsilon}^{\boldsymbol{el}}$ is the purely elastic deformation recoverable by unloading in the absence of damage. $\boldsymbol{\varepsilon}^{\boldsymbol{ed}}$ is the additional elastic deformation associated with the change of stiffness due to damage. According to Fig. 2:

$$\boldsymbol{\varepsilon}^{\boldsymbol{el}} = {\mathbf{D}_{\mathbf{T_0}}}^{-1} : \boldsymbol{\sigma}^{eq} \tag{14}$$

$$\boldsymbol{\varepsilon}^{\boldsymbol{ed}} = [\mathbf{D}_T(\boldsymbol{\Omega})^{-1} - {\mathbf{D}_{\mathbf{T_0}}}^{-1}] : \boldsymbol{\sigma}^{eq} \tag{15}$$

In which $\mathbf{D_{T_0}}$ is the undamaged thermo-elastic tensor. The increment of elastic deformation is split into a mechanical and a thermal component:

$$d\boldsymbol{\varepsilon}^{\boldsymbol{E}} = d\boldsymbol{\varepsilon}^{\boldsymbol{EM}} + d\boldsymbol{\varepsilon}^{\boldsymbol{ET}} \tag{16}$$

Within the proposed model formulation, crack-induced deformation can be deduced from the evolution law of damage [4], which is the only equation required at this stage to close the model formulation. As explained in Section 3.1, the damage flow rule is assumed to be associate, which means that the damage criterion is equal to the damage potential.

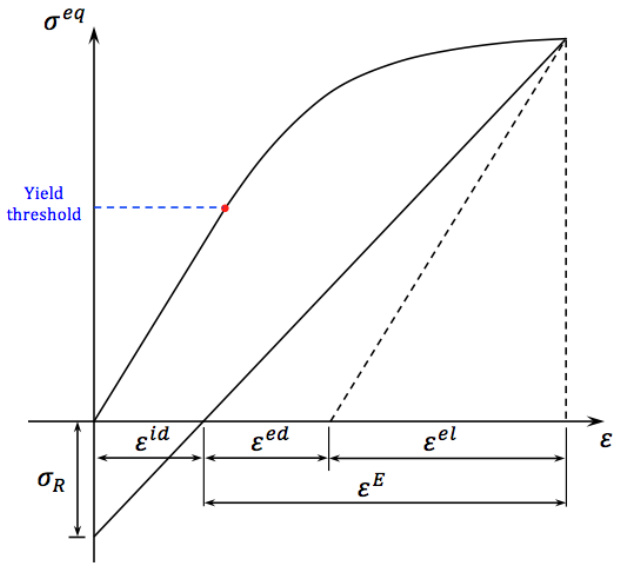

Fig. 2 Decomposition of total deformation (illustrated for a mechanical stress path). In the proposed model, total deformation is the sum of a purely elastic deformation ε^e (obtained in the absence of damage), a damaged elastic deformation ε^{ed} (additional elastic deformation induced by the loss of rigidity in damaged states), and an irreversible damage-induced deformation ε^{id} (due to residual crack opening). $\boldsymbol{\sigma}^{eq}$ is the equivalent stress, work-conjugate to total elastic strains

3.3 Damage criterion

Only certain components of the thermodynamic variable conjugate to damage ($\mathbf{Y}$) are expected to contribute to crack propagation, mainly: mechanical and thermal tensile stress maintaining cracks open after unloading. In addition, rock strength is expected to decrease with a temperature increase. The damage driving force component $\mathbf{Y_1}$ (Eq. 11b) is decomposed into:

$$\mathbf{Y_1} = \mathbf{Y_{1a}} + \mathbf{Y_{1b}} \tag{17a}$$

$$\mathbf{Y_{1a}} = -g\boldsymbol{\varepsilon}, \tag{17b}$$

$$\mathbf{Y_{1b}} = -\alpha(tr\boldsymbol{\varepsilon}^{\boldsymbol{E}})\boldsymbol{\varepsilon}^E - 2\beta(\boldsymbol{\varepsilon}^E \cdot \boldsymbol{\varepsilon}^E) \tag{17c}$$

$${\mathbf{Y_{1a}}}^{+} = -g\boldsymbol{\varepsilon}^{+} \tag{17d}$$

$${\mathbf{Y_{1a}}}^{-} = -g(\boldsymbol{\varepsilon} - \boldsymbol{\varepsilon}^{+}) \tag{17e}$$

When cracks propagate in mode I (i.e. when cracks open due to tension), ${\mathbf{Y_{1a}}}^{+}$ is the dominating damage-driving force. Note that ${\mathbf{Y_{1a}}}^{+}$ accounts for tensile deformation induced by mechanical stress or temperature increase (Eq. 16). $\mathbf{Y_2}$ (Eq. 11c) accounts for the change of rock properties due to temperature changes ($\mathbf{Y_2} = \mathbf{0}$ in a purely mechanical damage model). A quick dimensional analysis indicates that the term $\frac{1}{2\tau_0}\frac{\partial C(\boldsymbol{\Omega})}{\partial \boldsymbol{\Omega}}\tau^2$ can be neglected ($\frac{\partial C(\boldsymbol{\Omega})}{\partial \boldsymbol{\Omega}} \ll \frac{\partial [\mathbf{K}(\boldsymbol{\Omega})]}{\partial \boldsymbol{\Omega}} : \boldsymbol{\varepsilon}^E$). Note that inter-particle distance in rock increases with temperature. At higher temperatures, it requires more energy to separate rock crystals, which are already more distant than at

lower temperature. To capture this reduction of crack toughness (resulting in a reduction of rock strength) with temperature increase, and to counter-act the tensile damage-driving force $\mathbf{Y_{1a}}^+$, the following thermal damage driving force is defined as:

$$\mathbf{Y_2}^d = A \cdot \tau \cdot \alpha_T(\alpha + 2\beta) tr(\boldsymbol{\varepsilon}^{\boldsymbol{E}+}) \tag{18}$$

Where $\boldsymbol{\varepsilon}^{\boldsymbol{E}+}$ is the tensile elastic deformation, which indicates the increase of inter-particle distance at high temperature. A is a proportionality constant. Note that the expression in Eq. 18 is proportional to $\alpha_T(\alpha + 2\beta)\tau$, and varies like a polynomial of order one in elastic deformation, which is in agreement with the definition of the bulk modulus, and with Eqs. 5 & 11c. As a result, the total damage-driving force retained in the proposed thermo-mechanical damage model (noted $\mathbf{Y_d}^+$) is defined as:

$$\begin{aligned}\mathbf{Y_d}^+ &= \mathbf{Y_{1a}}^+ + \mathbf{Y_2}^d \\ &= -g\boldsymbol{\varepsilon}^+ + A \cdot \tau \cdot \alpha_T(\alpha + 2\beta) tr(\boldsymbol{\varepsilon}^{\boldsymbol{E}+})\end{aligned} \tag{19}$$

The damage criterion is expressed as the difference between the norm of the energy release rate and an energy threshold. The latter depends on damage (which plays the role of a hardening variable), in order to capture the increase of energy release rate with cumulated damage:

$$f_d(\mathbf{Y_d}^+, \boldsymbol{\Omega}) = \sqrt{\frac{1}{2}\mathbf{Y_d}^+ : \mathbf{Y_d}^+} - (C_0 + C_1\boldsymbol{\Omega}) \tag{20}$$

In which C_0 is the initial damage threshold which is necessary to trigger damage, and C_1 is a parameter which controls crack growth with cumulated damage. The increments of the Lagrange multiplier and of damage are calculated by using the consistency conditions (i.e., $f_d = 0$ and $\dot{f}_d = 0$):

$$d\lambda_d = -\frac{\frac{\partial f_d}{\partial \mathbf{Y_d}^+} : d\mathbf{Y_d}^+}{\frac{\partial f_d}{\partial \boldsymbol{\Omega}} : \frac{\partial f_d}{\partial \mathbf{Y_d}^+}} = \frac{\mathbf{Y_d}^+ : d\mathbf{Y_d}^+}{(C_1\delta) : \mathbf{Y_d}^+} \tag{21}$$

$$\begin{aligned}d\boldsymbol{\Omega} &= d\lambda_d \frac{\partial f_d(\mathbf{Y_d}^+, \boldsymbol{\Omega})}{\partial \mathbf{Y_d}^+} \\ &= \frac{[\frac{\mathbf{Y_d}^+}{\sqrt{2\mathbf{Y_d}^+ : \mathbf{Y_d}^+}}] : d\mathbf{Y_d}^+}{(C_1\delta) : [\frac{\mathbf{Y_d}^+}{\sqrt{2\mathbf{Y_d}^+ : \mathbf{Y_d}^+}}]} [\frac{\mathbf{Y_d}^+}{\sqrt{2\mathbf{Y_d}^+ : \mathbf{Y_d}^+}}]\end{aligned} \tag{22}$$

3.4 Unilateral effects of crack closure on damaged stiffness

The recovery of compression strength by the closure of tensile cracks is known as unilateral condition in CDM. In terms of stiffness, it can be expressed as [12]:

$$\begin{aligned}&\mathbf{D}_{\text{eff}}(\boldsymbol{\Omega}) = \mathbf{D}(\boldsymbol{\Omega}) \\ &+ \eta \sum_{i=1}^{3} H(-tr(\mathbf{P_i} : \boldsymbol{\varepsilon}))\mathbf{P_i} : (\mathbf{D}_0 - \mathbf{D}(\boldsymbol{\Omega})) : \mathbf{P_i}\end{aligned} \tag{23}$$

In which $\mathbf{D}_{\text{eff}}(\boldsymbol{\Omega})$ is the "partially recovered" stiffness tensor. $\mathbf{P_i}$ is the fourth order projection tensor (projection in crack planes normal to principal direction i). H is the Heaviside function. η is a parameter that indicates the degree of maximum stiffness recovery ($0 < \eta \leq 1$). In the following simulations, it is assumed that stiffness is fully recovered as soon as cracks are closed under compression (i.e., $\eta = 1$).

4 Parameter calibration, model verification and sensitivity analysis

The advantage of the model proposed above is that the number of parameters required is minimal (seven mechanical parameters: λ, μ, α, β, g, C_0, C_1; and one thermal parameter: α_T). Published data sets on thermo-mechanical behaviour of both sandstone and granite are available in the literature [34, 55, 79, 84]. However, most of the data is analyzed within the framework of thermo-elasticity, and there is not enough evidence on stiffness weakening and irreversible deformation induced by temperature gradients to really verify the proposed model against experimental data. According to experimental studies published in [28, 29], the proposed thermo-mechanical damage model is expected to provide good predictions of tight rock macroscopic failure induced by crack opening and closure. Many authors used a similar mechanical damage model for sandstone, even though other mechanisms such as grain crushing and pore collapse are expected to drive macroscopic failure in porous rock. The proposed model is seen as a versatile framework, that can be used to capture the loss of energy induced by damage in any rock material, provided that model parameters are well calibrated. In order to assess the performance of the model in doing so, calibration and verification simulations were performed on sandstone, for which experimental data was found in [77] (drained triaxial compression tests on saturated sandstone). Reference stress/strain curves for this calibration were obtained for a confining pressure of 40 MPa. The triaxial tests used for model verification purposes were performed for confining pressures amounting to 28 MPa and 50 MPa. The corresponding stress/strain curves are displayed in Fig. 3. Note that the soil mechanics sign convention was adopted throughout the paper (with compression counted positive).

The plots obtained for the verification tests (at 28 MPa and 50 MPa) show that the model predictions match experimental data with an error less than 5% before the peak of stress. This is considered as a satisfactory result, since the purpose of this study is to predict the effect of thermo-mechanical crack opening and closure before softening. Due to the thermo - elastic framework adopted in the proposed model (Eq. 4), the expression of the damaged thermo - mechanical stiffness $\mathbf{K}(\boldsymbol{\Omega})$ results from the expression of the

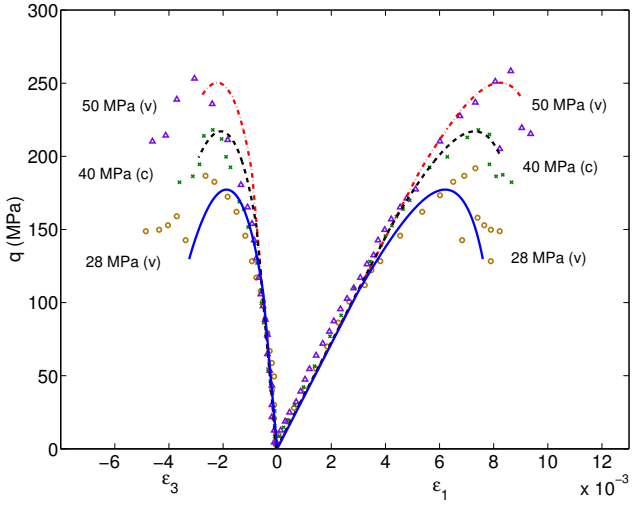

Fig. 3 Stress/strain curves obtained during drained triaxial compression tests conducted on saturated sandstone: the dots are reported experimental data found in [77]; solid and dashed lines represent the results of simulations performed in MATLAB with the proposed damage model. The curve used for model calibration (c) corresponds to the test performed under a confining pressure of 40 MPa. Simulations for model verification (v) were performed for confining pressures of 28 MPa and 50 MPa

damaged stiffness tensor, so that the thermal expansion coefficient α_T can be considered as a purely thermo-elastic parameter - not a damage parameter. That is the reason why in the present study, α_T was assigned a value known to be a standard for rock materials (negative with the soil mechanics sign convention). Table 3 summarizes the parameters obtained for sandstone after calibration and verification - referred to as the parameters of "Type I sandstone" in the following.

Table 3 Model parameters obtained for Type I sandstone after calibration and verification (with the soil mechanics sign convention)

λ (Pa)	μ (Pa)	α (Pa)	β (Pa)
8.13×10^{9}	1.53×10^{10}	1.2×10^{10}	-4×10^{10}
g (Pa)	C_0 (Pa)	C_1 (Pa)	α_T ($^\circ K^{-1}$)
1.17×10^{8}	700	3.8×10^{5}	-1×10^{-5}

A sensitivity analysis is now carried out in order to explain the physical meaning of the five mechanical damage parameters (α, β, g, C_0, C_1). Strain controlled triaxial compression tests were simulated (for a confining pressure of 15 MPa). The initial damage threshold C_0 was used as a scaling factor. The values of the normalized damage parameters (α/C_0, β/C_0, g/C_0, C_1/C_0) were first assigned a value according to the calibration study published in [28] for sandstone (for reference, the set of constitutive parameter is reported in Tab. 4). Each normalized parameter was then varied one by one, keeping all the other parameters constant (Fig. 4). Larger α and β values imply a more ductile behavior, as can be seen from the portion of the stress-strain curve corresponding to higher deformation (Fig. 4a&b). As g increases, the irreversible deformation and corresponding residual stress increase. So the peak of the stress-strain curve tends to shift downward (Fig. 4c). C_1 has an influence on the strain hardening portion as damage starts to accumulate (Fig. 4d).

Table 4 Reference set of constitutive parameters used in the sensitivity analysis (after [28])

λ (Pa)	μ (Pa)	α (Pa)	β (Pa)
2.63×10^{10}	1.75×10^{10}	1.9×10^{9}	-2.04×10^{10}
g (Pa)	C_0 (Pa)	C_1 (Pa)	α_T ($^\circ K^{-1}$)
1.1×10^{8}	1×10^{3}	5.5×10^{5}	-1×10^{-5}

5 Analysis of thermo-mechanical stress paths

5.1 Simulation of thermo-mechanical crack opening

The thermo-mechanical damage model presented in Section 3 was used to simulate crack-induced damage during a triaxial compression test comprising a thermo-mechanical loading phase, for the Type I sandstone studied in Section 4. The energy released to propagate damage in a sample under mechanical compression is compared to the energy released to propagate damage in a sample subject to heating under zero axial strain. Such an analysis can be used to study underground rock pillars subjected a rapid temperature increase caused by a fire or an explosion. Three loading phases are considered:

(M1) *Isotropic compression.* An isotropic confining pressure (of 20 MPa) is applied under stress-controlled conditions. The confining pressure is chosen so as to ensure that the damage criterion is not reached: during this phase, the material remains elastic.

(M2) *Triaxial compression.* The sample is loaded by increasing the axial strain (direction 1) at a constant strain rate (so as to reach a maximal axial strain of 0.00226). The lateral stresses do not change throughout this phase.

(TM) *Confined heating.* Axial deformation is fixed while the temperature is increased by $150\,^\circ K$ from the initial room temperature (assumed $293\,^\circ K$). Lateral stresses are fixed, which means that lateral expansion can occur.

Two sequences are simulated (Fig. 5):

(1) $M1 \rightarrow M2 \rightarrow TM$;

(2) $M1 \rightarrow TM \rightarrow M2$.

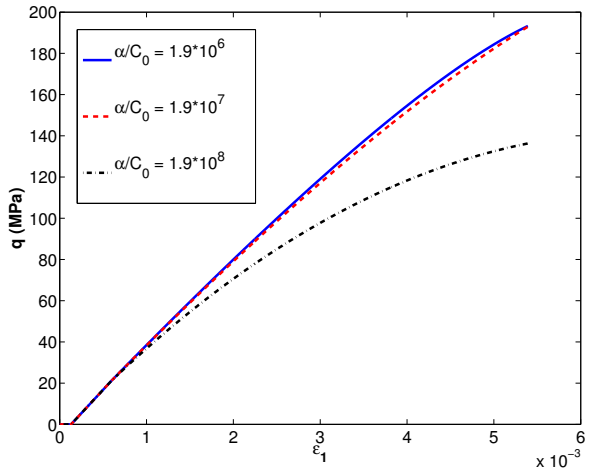

(a) Effect of α

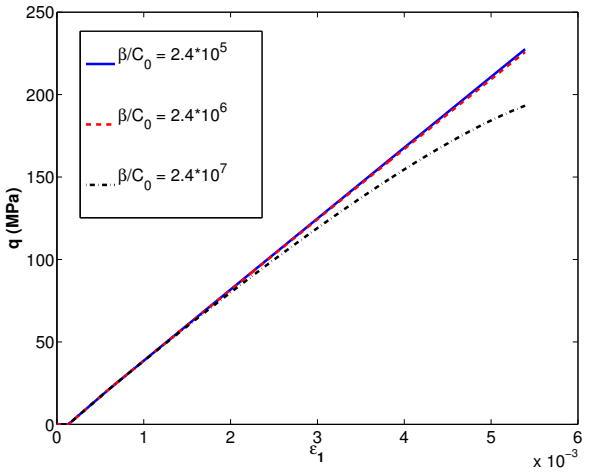

(b) Effect of β

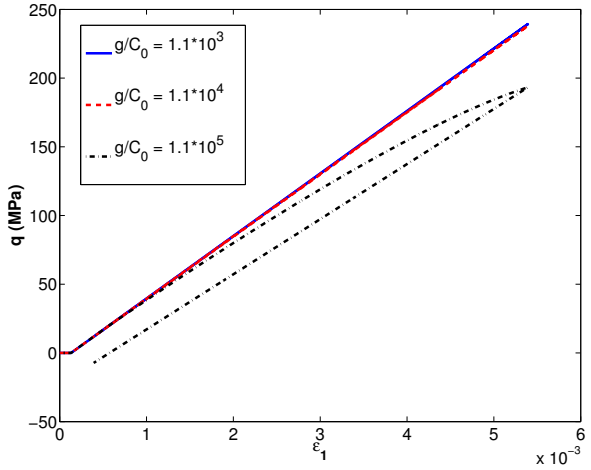

(c) Effect of g

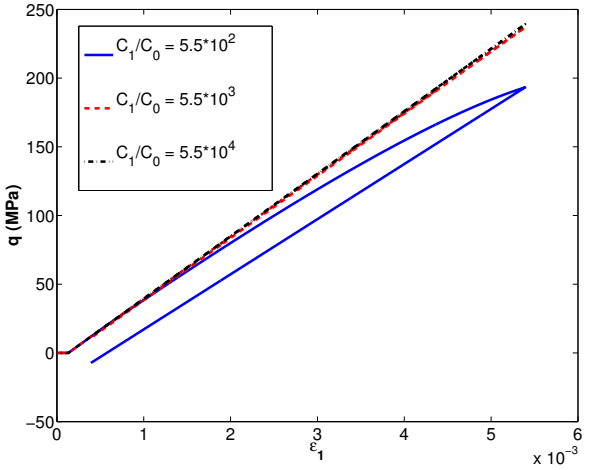

(d) Effect of C_1

Fig. 4 Sensitivity analysis on the mechanical damage parameters used in the model (all expressed in units of pressure). C_0: initial damage threshold; C_1: hardening parameter; α & β: parameters controlling the shape of the damaged stress/strain curve (ductile vs. brittle trends)

During the triaxial compression phase (M2), deviatoric stress q generates lateral tensile strain, causing lateral damage ($\Omega_1 = 0$, $\Omega_2 = \Omega_3 \neq 0$). Correspondingly, a degradation of rock stiffness is observed, in both stress-strain curves (AB_1 & B_2C_2 in Fig. 6a). For both sequences, q increases with temperature (AB_2 & B_1C_1 in Fig. 6a). This is due to the mechanical boundary conditions: axial thermal expansion is constrained, which generates compressive internal stress in virtue of the action/reaction principle. Temperature-induced compression adds to mechanical compression. Damage induced during the mechanical phase AB_1 (axial compression) lowers stiffness, which explains why the thermal compressive stress developed in reaction to thermal expansion during the heating phase B_1C_1 (sequence 1) is smaller than during the heating phase AB_2 (sequence 2) (Fig. 6a).

The 3D plot in Fig. 6b shows the evolution of damage for the stress paths simulated in the two sequences described above. Fig. 6c and 6d are projections in the strain-damage and temperature-damage spaces, respectively. Overall, less damage occurs in sequence 2. This could be expected from the model formulation: in sequence 2, a mechanical loading is applied to a heated material, in which the "counter-acting" damage driving force $\mathbf{Y_2}^d$, accounting for the decrease of rock strength with temperature increase (Eq. 18), is larger than in sequence 1. As a result, the cumulated damage driving force $\mathbf{Y_d}^+$ (Eq. 19) in sequence 2 is smaller than in sequence 1 - in other words, less energy is released to open cracks in sequence 2. Moreover, Fig. 6c indicates that lateral damage progresses faster in a cooler sample (slope $A'B_1$ $>$ slope B_2C_2; segment AA' represents the purely elastic range).

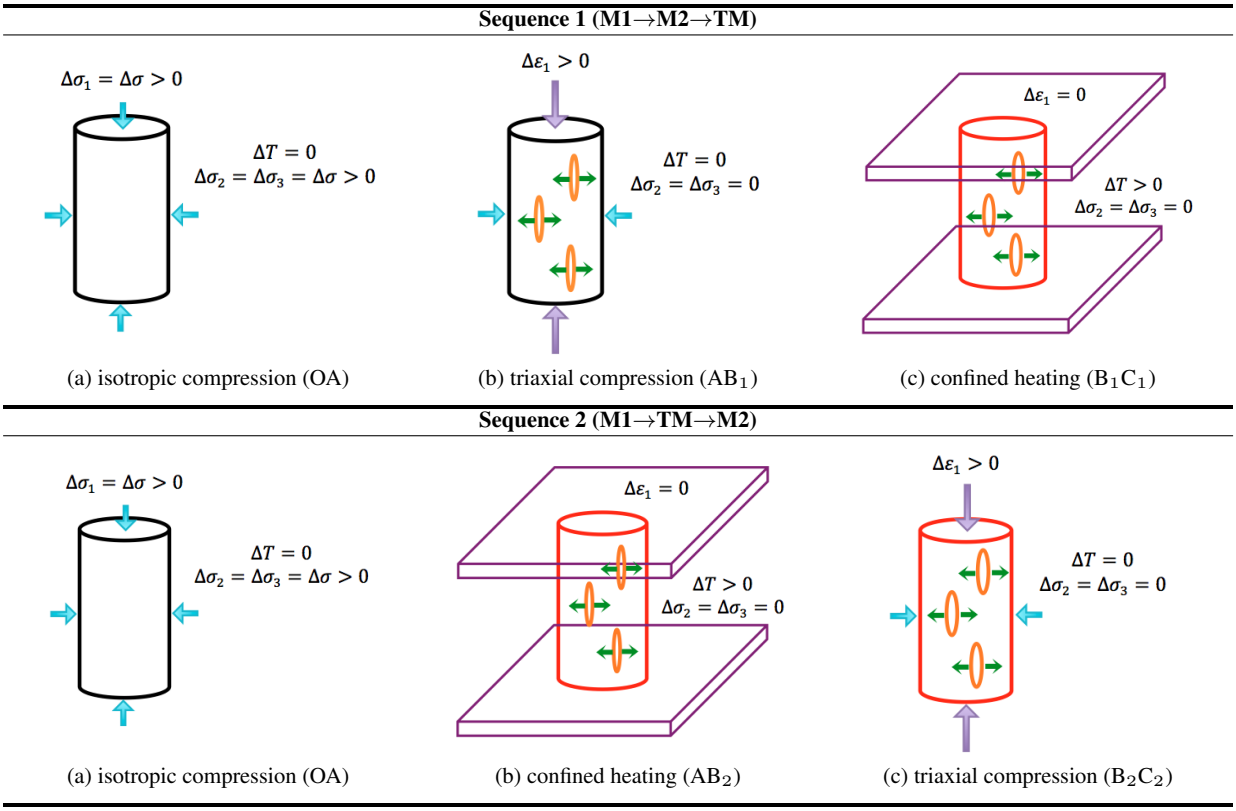

Fig. 5 Stress paths simulated to study the influence of thermo-mechanical crack opening: comparison of mechanical and thermo-mechanical energy released during the propagation of compression damage

In both sequences, the sample expands laterally (due to mechanical or thermo-mechanical compression). As expected, larger damage results in larger deformation, and lateral strains (ε_3) obtained at the end of sequence 1 are larger than at the end of sequence 2 (Fig. 6c). In sequence 1, damage induced by mechanical compression increases the minimum energy release rate (Eq. 20) required to further propagate cracks in the heating phase (slope of B_1C_1 < slope of OB_1 in Fig. 6c for ε_3). On the other hand, for sequence 2, the damage threshold (i.e. the energy required to propagate cracks) increases with both thermo-mechanical stress and higher ambient temperature. As a result, slope of B_2C_2 is smaller than OB_2 (Fig. 6c). In the undamaged material, there is a damaged temperature threshold, below which thermo-mechanical cracks will not develop - the temperature threshold is about $427\,°K$ for the Type I sandstone under study (OAA′, Fig. 6d). However, if mechanical cracks have been produced before heating the sample, any increase in temperature will immediately cause damage to propagate in the sample (B_1C_1, Fig. 6d).

5.2 Simulation of thermo-mechanical crack closure

The thermo-mechanical damage model presented in Section 3 was used to simulate the evolution of damage in a sample of Type I sandstone, during a uniaxial tension test followed by a compression induced by either mechanical or thermo-mechanical stresses. Deep underground tunnels need to be cooled before being exploited for mining, which raises some interest in studying potential crack closure due to cooling in rock subject to displacement boundary conditions. The stress path (Fig. 7) was as follows:
(1) *Uniaxial tension:* crack opening (OA-AB). The sample is loaded by increasing the axial tensile strain (direction 1) at a constant strain rate ($\Delta\varepsilon_1$), up to $\varepsilon_1 = -0.00016$. Temperature and lateral stresses are kept constant ($\Delta\sigma_2 = \Delta\sigma_3 = 0$, $\Delta T = 0$). Crack planes perpendicular to the axis are produced due to the tensile stress.
(2) *Mechanical "relaxation"*: release of tensile stress (BC). The sample is unloaded in order to release the tensile stresses completely. The unloading process is elastic (linear stress / strain plot), and only the elastic part of crack-induced deformation is compensated (at the end of this loading phase: $\varepsilon^{ed} = 0$, but $\varepsilon^{id} \neq 0$).

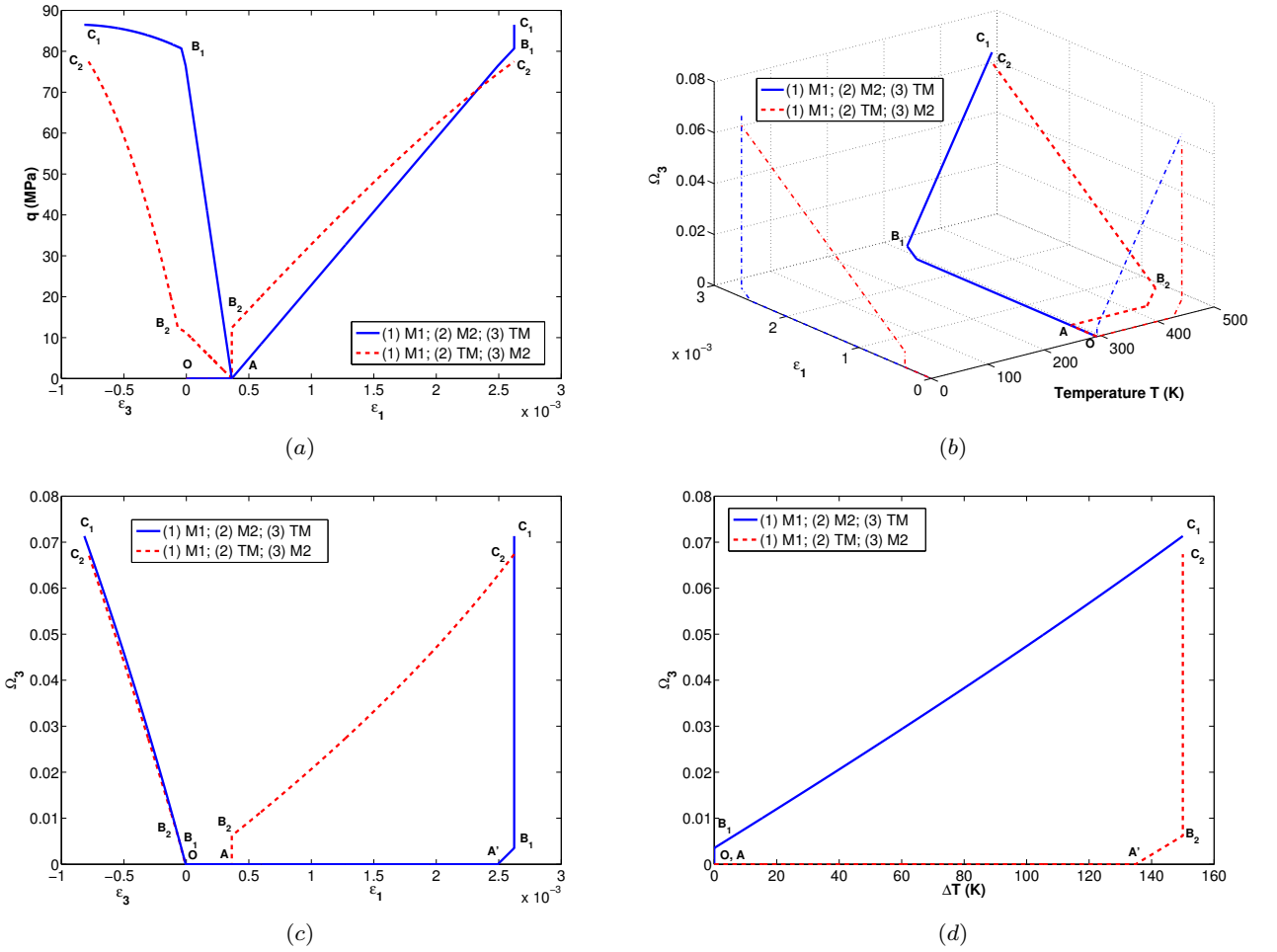

Fig. 6 Simulation of the two thermo-mechanical stress paths described in Fig. 5 (confining pressure: 20 MPa; maximum axial strain: 0.00226; maximum temperature change: 150 $^\circ K$): (a) Deviatoric stress vs. axial and lateral deformation; (b) Damage evolution vs. axial deformation and temperature variation; (c) Damage evolution vs. axial and lateral deformation; (d) Damage evolution vs. temperature variation

(3) *Compression* (CD-DE). Two stress paths are considered to study unilateral effects induced by crack closure:

a. decrease of temperature (ΔT = -60 $^\circ K$) with zero axial deformation,
b. purely mechanical axial compression at constant temperature.

The present analysis focuses on opening and closure of one family of cracks perpendicular to the axis of loading. To avoid the formation of axial cracks, compression in the third loading phase was kept below the compressive strength of the material considered (Fig. 7). During cooling (3a, Fig. 7), mechanical boundary conditions were applied: the sample was free to contract laterally, but not axially ($\Delta\varepsilon_1 = 0$, $\Delta\sigma_2 = \Delta\sigma_3 = 0$). Consequently, internal tensile forces developed in the undamaged part of the sample (i.e., outside the cracks). In virtue of the principle of action and reaction, cracks closed due to the internal compression forces acting at crack faces (3a, Fig. 7 and CD_1, Fig. 8b). In the mechanical compression phase (3b, Fig. 7), further compressive strain was applied at a constant rate ($\Delta\varepsilon_1$) under constant lateral stress ($\Delta\sigma_2 = \Delta\sigma_3 = 0$).

Rock tensile strength is relatively low, so that damage starts to develop quickly after the tensile load is applied. Correspondingly, the stress-strain curve is linear on a very short interval (OA, Fig. 8a), which is followed by a nonlinear response (AB, Fig. 8a) associated to the development of damage (AB, Fig. 8c). The stress/strain curve compares satisfactorily with the experimental results obtained for a direct tension test, reported in [64]. During the stress release phase, the sample is unloaded elastically. Pure elastic deformation (ε^{el}) and damage-induced elastic deformation (ε^{ed}) are recovered (BC, Fig. 8a). During this phase, damage does not evolve (BC, Fig. 8c).

When cracks are completely closed, unilateral effects induce an increase of stiffness, thus, an increase of the bulk

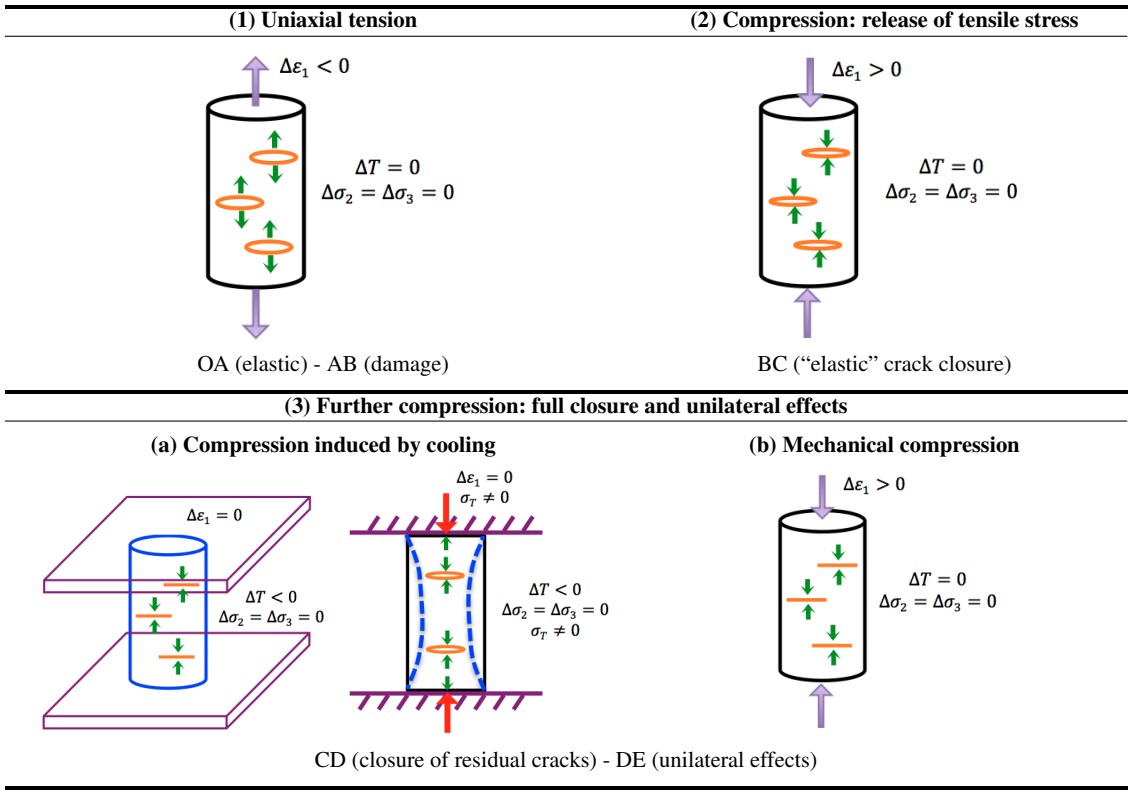

Fig. 7 Stress paths simulated to study the influence of thermo-mechanical crack closure: comparison of mechanical and thermo-mechanical compression loadings

modulus (slope D_1E_1, Fig. 8b). If cracks are closed by cooling, lateral deformation is a contraction, and the sum of thermal and mechanical axial deformation is zero (so that OC = OD'_1 in Fig. 8a & 8b). Consequently, the damage-driving force defined in Eq. 19 remains constant. As a result, damage does not increase (C-D_1-E_1, Fig. 8c). If cracks are closed by mechanical compression, unilateral effects are observed once cracks are completely closed (i.e. $\varepsilon = 0$). The slope (CD_2) of the stress/strain diagram in stage 3 is the same as in stage 2 (BC) (Fig. 8d) because tensile deformation still exists. The slope of the stress/strain diagram becomes steeper when deformation is negative (D_2E_2, Fig. 8d) and is actually equal to the slope of OA (characteristic of the undamaged material).

The combined plots shown in Fig. 8d reveal that both thermo-mechanical and purely mechanical processes can completely close the residual cracks. Note that the slope of the stress/strain curve after crack closure is steeper for the thermal closure mechanism (slope of D_1E_1 -for cooling) than for the mechanical closure mechanism (slope of D_2E_2 - for compression), i.e. for the elastic moduli and thermal expansion parameters of Type I sandstone, mechanical axial compression produces more axial deformation (ε_1) than cooling. The stress/strain diagrams also show that the strain energy needed to close residual cracks by mechanical compression is slightly larger than the energy needed to close residual cracks by cooling. In other words, mechanical compression is less work-efficient than cooling to close the cracks.

6 Comparison of the thermo-mechanical responses of different rocks

The thermo-mechanical damage model presented in Section 3 is now used to compare the thermo-mechanical response of three rocks, described in Tables 5 and 6. Note that these three rocks (two sandstones, one granite) are different from the sandstone used for the model calibration (presented in Section 4). The objective of this parametric study is not to compare the brittle response of different rocks: the following simulations were performed in order to link sets constitutive parameters defined at the REV scale (Tab. 6) to specific rock fabrics (Tab. 5). This type of analysis is expected to facilitate statistical model calibration in future studies (by ignoring certain damage parameters that may be irrelevant for certain rocks, or by better initializing the relative orders of magnitude between damage parameters). Stress paths similar to the ones described in Section 5 are simulated, as follows:

– *Test 1: thermo-mechanical crack opening*: (M1) isotropic compression up to 20 MPa; (M2) strain-controlled axial

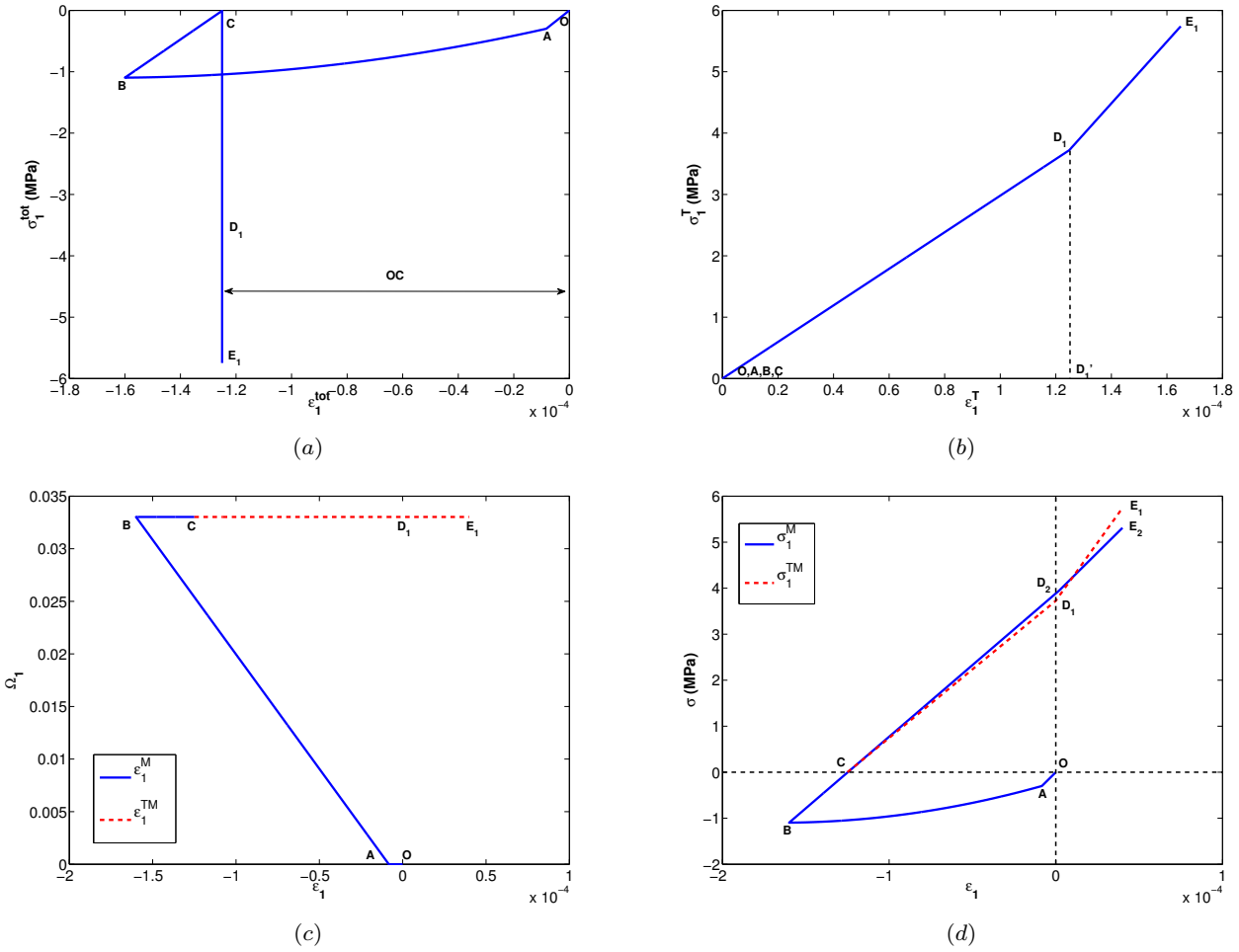

Fig. 8 Simulation of the thermo-mechanical stress paths described in Fig. 7: (a) total stress vs. axial deformation (crack closure by cooling); (b) thermal stress vs. thermal strain: length of OC equals to length of OD_1'(crack closure by cooling); (c) evolution of axial damage (direction 1) vs. axial deformation (TM – closure by cooling; M – closure by compression); (d) evolution of stress components with axial deformation (TM – closure by cooling; M – closure by compression)

compression up to $\varepsilon_1 = 0.00726$; (TM) temperature increase of $150\,^\circ K$.

- *Test 2: thermo-mechanical crack opening*: (M1) isotropic compression up to 20 MPa; (TM) temperature increase of $150\,^\circ K$; (M2) strain-controlled axial compression up to $\varepsilon_1 = 0.00726$.
- *Test 3: thermo-mechanical crack opening*: (M1) isotropic compression up to 20 MPa; (TM) temperature increase of $450\,^\circ K$; (M2) strain-controlled axial compression up to $\varepsilon_1 = 0.00726$.
- *Test 4: thermo-mechanical crack closure*: (1) strain- controlled uniaxial tension up to $\varepsilon_1 = -0.00015$; (2) relaxation of axial tensile stress; (3) decrease of temperature ($\Delta T = -60\,^\circ K$) with zero axial deformation.
- *Test 5: thermo-mechanical crack closure*: (1) strain- controlled uniaxial tension up to $\varepsilon_1 = -0.00015$; (2) relaxation of axial tensile stress; (3) purely mechanical axial compression at constant temperature.

As mentioned earlier, the theoretical model presented in Section 3 depends on seven mechanical parameters (λ, μ, α, β, g, C_0, C_1) and one thermal parameter (α_T). The simulations presented below were performed with a standard value for the thermal expansion coefficient (α_T), which, according to the model formulation, does not depend on damage. The values of the mechanical parameters were calibrated against experimental data elsewhere [23, 29, 70], and used as such in the following parametric study (Table 6). Note that the calibration process used by the authors cited in Table 6 is not straightforward. In fact, any data point provided by the experimental stress/strain curve adds not only one equation, but also one unknown (the value of current damage at that point). As a result, an iterative calibration technique was proposed by Halm and Dragon [23]. The elastic constants λ

and μ are determined from the initial Young's modulus E_0 and initial Poisson's ratio ν_0 in the elastic region ($f_d < 0$) of the stress/strain curve. The subsequent non-elastic loading and elastic unloading portions are then used to get the values of $\alpha\Omega_3$, $\beta\Omega_3$, and $g\Omega_3$ (where Ω_3 stands for the lateral damage developing during a triaxial compression test). The axial deformation measured when damage first occurs provides the initial damage threshold. Another point of the stress/strain curve can be used at the beginning of the unloading phase, in order to relate the parameters C_0 and C_1 to g. Iterations are required to identify the most appropriate value for Ω_3. By this means, the set of material parameters can be determined from a single loading-unloading triaxial compression stress path.

Results obtained for the three types of rock during tests 1 and 2 (resp. test 3) are displayed in Fig. 9 (resp. Fig. 10). In tests 1 and 2, the sample expands laterally (due to mechanical or thermo-mechanical compression). As noted earlier in Section 5.1, the energy that needs to be released to open cracks during the heating phase is larger in test 1 than in test 2, because of damage hardening. As a result, thermal damage is observed for a lower temperature increase in test 2 (Fig. 9$c_1\&c_2$). Like in the test performed on Type I sandstone (Section 5.1), the total amount of damage produced in test 1 exceeds the total amount of damage obtained in test 2 (Fig. 9 $b_1\&b_2$). In this particular parametric study, Type III sandstone (resp. granite) is the least (resp. most) brittle material amongst the three rocks tested (Fig. 9 $a_1\&a_2$). Type II sandstone undergoes more damage than the two other types of rocks. It is worth noticing that the three materials do not rank in the same order for stiffness and strength (Fig. 9 $a_1\&a_2$) and for damage development (Fig. 9 $b_1\&b_2$). Type II sandstone may serve as a mechanical shield in an underground facility (high stiffness even in damaged states), but Type III sandstone may be a better barrier against leakages (low crack density). In addition, Fig. 10 shows that if test 2 is conducted with a temperature increase of $450\,^\circ K$ instead of $150\,^\circ K$ (test 3 described above), cumulated damage can reach a similar value as in test 1. In other words, in order to crack the rock as much as in the loading sequence 2 (Fig. 5), it is necessary to multiply the temperature increase by about three during the heating phase preceding the mechanical loading phase.

In tests 4 and 5 (extension followed by relaxation and closure by cooling or compression), the plots are positioned in the same order as in tests 1, 2 and 3. Type II sandstone is the most damaged rock (Fig. 11c), granite is the most brittle, and Type III sandstone is the most ductile (Fig. 11 $a\&b$). Note that for the material parameters adopted (Table 6), granite tensile strength turns out to be of the order of 60 MPa (Fig. 11a), whereas reference values reported for granite tensile strength are in the range of 7 to 25 MPa [34]. The constitutive parameters used for the simulations were calibrated by other authors from stress/stress curves obtained in triaxial compression tests. The discrepancy observed for granite tensile strength suggests that the calibration data set should be complemented by experimental results from tensile tests. Fig. 12 shows the stress/strain curves obtained for the three rocks under study. In test 5 (mechanical compression closes the cracks), the slope of the curve comes back to its initial value (virgin material) as soon as deformation is compressive (positive with the soil mechanics sign convention). In test 4, the three rocks exhibit different behavior upon closure of the cracks during the cooling phase. Type II sandstone tends to harden during the closure phase, i.e. the point at zero deformation is reached for a higher total compressive stress than for the compression closure mechanism (Fig. 12a). On the contrary, Type III sandstone tends to soften during the closure phase, i.e. the point at zero deformation is reached for a (slightly) lower total compressive stress than for the compression closure mechanism (Fig. 12b). Granite is only affected by temperature changes after full crack closure: after the point at zero deformation has been reached, the slope of the stress/strain curves becomes equal to the slope of the thermo-mechanical loading curve of the virgin material - steeper than the slope of the mechanical loading curve (Fig. 12c).

7 Conclusions

Temperature plays a central role in rock mechanics: temperature variations can induce pore fluid phase changes, as well as microstructure changes. In salt rock for instance, ambient temperature dictates the creep mechanisms originating damage and healing. Thermal gradients, combined to mechanical boundary conditions (e.g., constrained displacement at a tunnel support, fixed stress value in the far field) can also induce cracking due to thermal stress concentrations. The latter influences energy release rates in the same way as pure mechanical stress concentrations calculated in fracture mechanics. The literature review presented in the first part of this paper summarizes observations made in the laboratory during thermo-mechanical stress paths imposed to different types of rock, and provides an overview of the constitutive models proposed within the framework of Continuum Damage Mechanics.

Following that framework, the thermodynamic model proposed herein aims to predict stiffness anisotropy induced by thermo-mechanical crack opening and closure in rock. Damage is defined as the second-order crack density tensor [45]. Halm and Dragon's model [28] is used as a basis to postulate the form of the free energy, which is expressed in the form of a polynomial of deformation, temperature and damage. Thermo-elastic energy potentials are made dependent on damage - by assuming that in addition to the bulk modulus, heat capacity is affected by damage. Stress and the

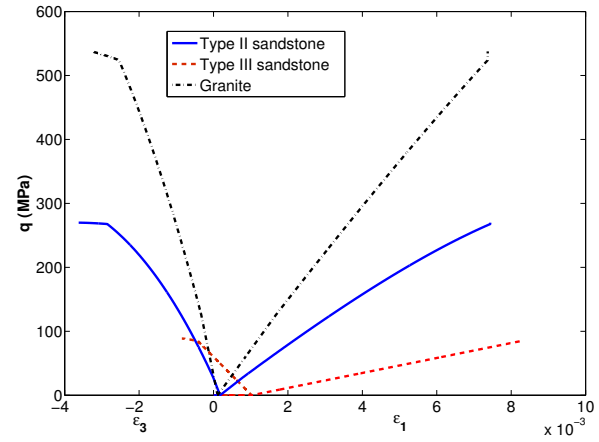

(a_1) Test 1: deviatoric stress vs. deformation.

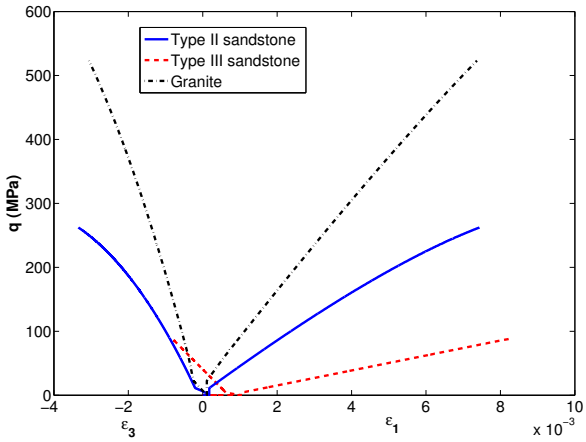

(a_2) Test 2: deviatoric stress vs. deformation.

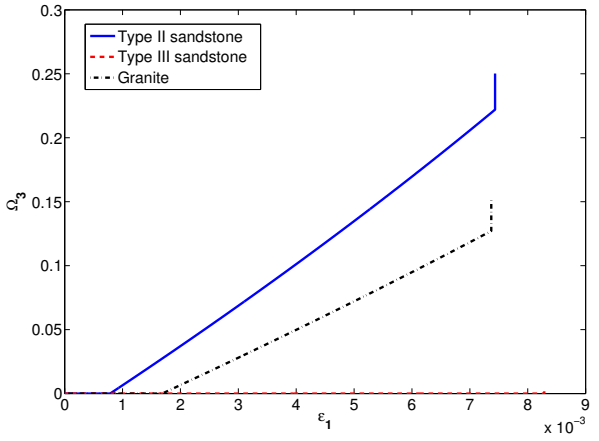

(b_1) Test 1: lateral damage vs. axial deformation.

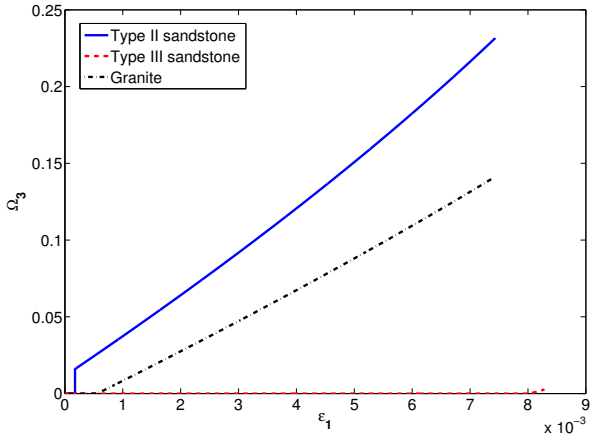

(b_2) Test 2: lateral damage vs. axial deformation.

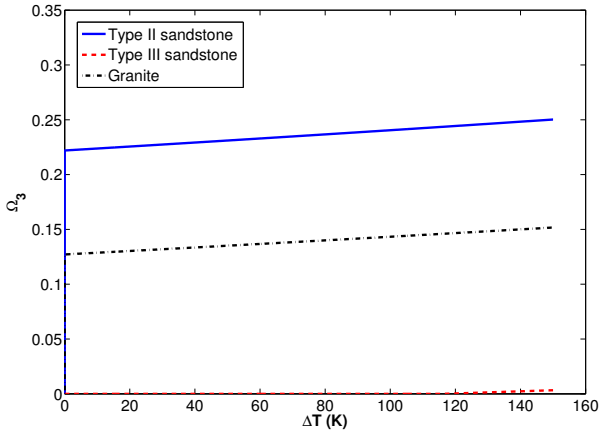

(c_1) Test 1: lateral damage vs. temperature change.

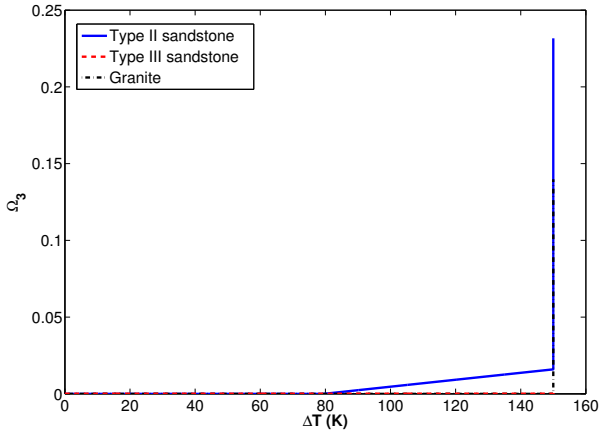

(c_2) Test 2: lateral damage vs. temperature change.

Fig. 9 Simulation of thermo-mechanical crack opening for three types of rock: in test 1, damage propagates first due to the mechanical loading, and then due to the temperature increase; in test 2, damage propagates first due to the temperature increase, and then due to the mechanical loading. In order to compare the effect of the loading sequence, the same mechanical and thermal loads were used in both tests

Table 5 Microscopic characteristics and macroscopic properties of the rocks chosen for the parametric study (σ_3 = confining pressure, ε_p = strain when stress reaches its peak value)

Rock	Main mineral	Grain size (μm)	Porosity (%)	Peak stress	References
Type II sandstone	98% quartz	250	21	130 MPa (σ_3 = 14 MPa, ε_p= 0.0055)	[23, 77]
Type III sandstone	93% quartz, some feldspar and mica	150 $\sim$ 450	22	93 MPa (σ_3 = 20 MPa, ε_p= 0.01)	[5, 70]
Granite	feldspar, biotite	2000 $\sim$ 8000	0.3 $\sim$ 0.4	320 MPa (σ_3 = 20 MPa, ε_p= 0.0046)	[29, 33]

Table 6 Thermo-Mechanical constitutive parameters used in the parametric study, calibrated against experimental data by other authors

Rock	λ (Pa)	μ (Pa)	α (Pa)	β (Pa)	g (Pa)	C_0 (Pa)	C_1 (Pa)	$\alpha_T (K^{-1})$
Type II sandstone [23]	2.63×10^{10}	1.75×10^{10}	1.9×10^{9}	-2.04×10^{10}	1.1×10^{8}	1×10^{3}	5.5×10^{5}	-1×10^{-5}
Type III sandstone [70]	3.25×10^{9}	4.88×10^{9}	9.93×10^{9}	-1.12×10^{10}	3.2×10^{7}	2×10^{4}	2.7×10^{5}	-1×10^{-5}
Granite [29]	3.99×10^{10}	3.13×10^{10}	-1.6×10^{10}	-3.1×10^{10}	3.3×10^{8}	1.1×10^{5}	2.2×10^{6}	-1×10^{-5}

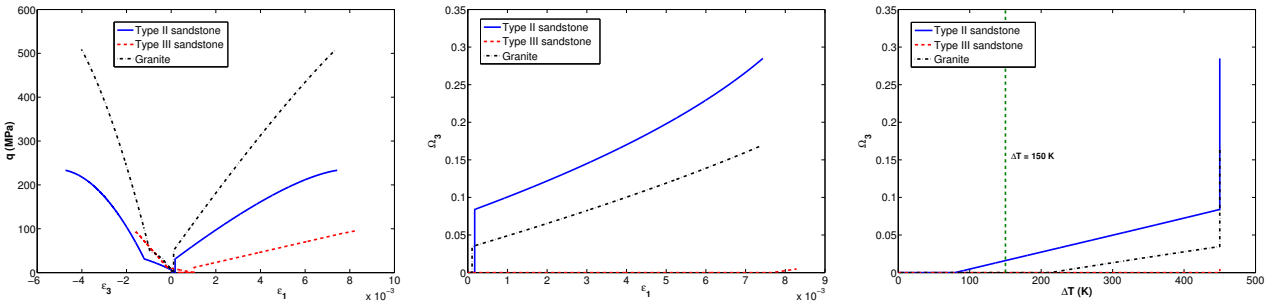

(a) Deviatoric stress vs. deformation. (b) Lateral damage vs. axial deformation. (c) Lateral damage vs. temperature increase.

Fig. 10 Thermo-mechanical crack opening (Test 3): (M1) isotropic compression up to 20 MPa; (TM) temperature increase of 450 $^\circ K$; (M2) strain-controlled axial compression up to $\varepsilon_1 = 0.00726$

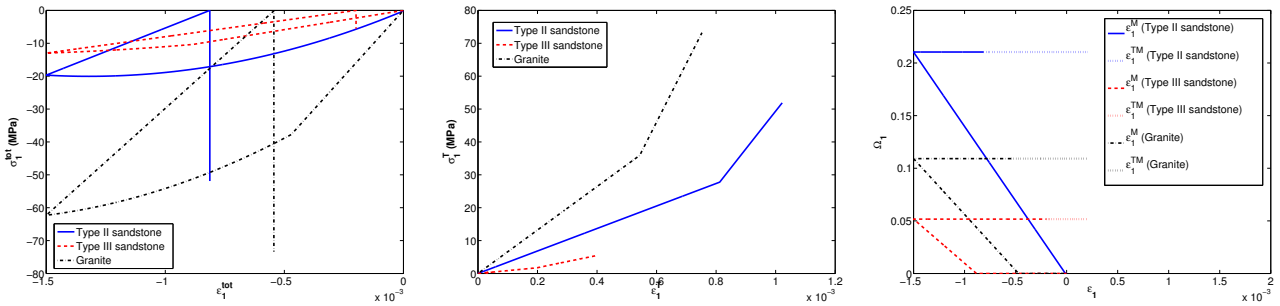

(a) Axial stress vs. axial deformation. (b) Thermal axial stress vs. axial thermal deformation. (c) Axial damage vs. axial deformation.

Fig. 11 Thermo-mechanical crack closure for the three rocks selected for the parametric study (Tests 4 and 5): (a) total stress vs. axial deformation (crack closure by cooling); (b) thermal stress vs. thermal strain (crack closure by cooling); (c) evolution of axial damage (direction 1) vs. axial deformation (see also Fig. 8c)

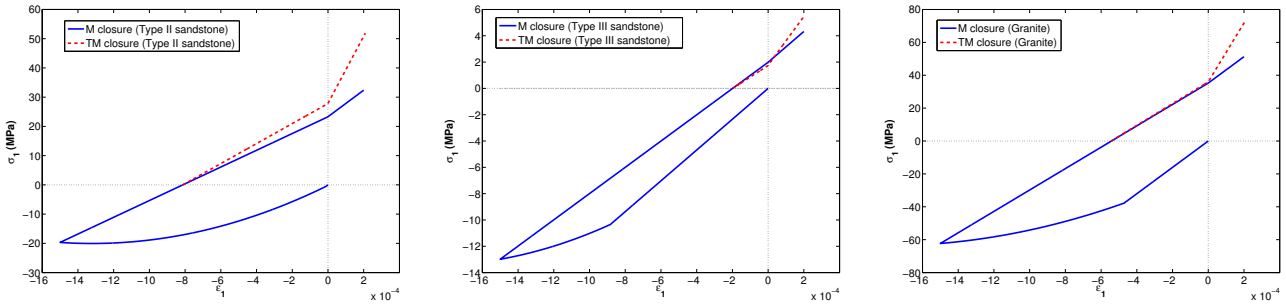

(*a*) Type II Sandstone. (*b*) Type III Sandstone. (*c*) Granite.

Fig. 12 Thermo-mechanical crack closure for the three rocks selected for the parametric study (Tests 4 and 5): axial stress vs. axial strain

damage-driving force are derived from the free energy, and conjugation relationships indicate that stress and damage driving force depend on internal variables (such as damage) and external variables (e.g., strain and temperature). The energy release rate controlling damage propagation is a modified damage-driving force. The damage criterion controls mode I crack propagation, captures temperature-induced decrease of rock strength, and accounts for the increase of energy release rate necessary to propagate cracks in a damaged medium. Crack closure is modeled through unilateral effects produced on rock stiffness. The thermo-mechanical damage model was calibrated and verified against experimental stress/strain curves obtained by Sulem and Ouffroukh [77] during drained triaxial compression tests conducted on saturated sandstone.

The set of calibrated constitutive parameters was then used to simulate the evolution of stiffness, deformation, damage and released energy for various stress paths. Crack opening induced by thermo-mechanical stresses was studied by simulating a triaxial compression test conducted in three phases: (1) an isotropic confining phase followed by an axial compression, followed by a heating phase; or: (2) an isotropic confining phase followed by a heating phase, followed by an axial compression. Results show that under anisotropic mechanical boundary conditions, cracks can be produced during heating. Higher ambient temperature increases the lateral expansion and produces more damage. In the proposed formulation, the thermo-mechanical energy release rate not only increases with thermal dilation, but also decreases with ambient temperature. If heating is applied before the mechanical compression load, there is a temperature threshold, below which the rock behaves elastically. Thermo - mechanical crack closure was studied by simulating a uniaxial tension test followed by a stress relaxation phase, followed by a compression phase: (1) either by cooling with fixed axial displacements, (2) or by mechanical axial compression. The degradation of stiffness due to tensile stress and recovery of stiffness due to unilateral effects are well captured. The simulation of the confined cooling phase also illustrates the capability of the model to predict crack closure induced by coupled thermo-mechanical stresses.

A parametric study was performed to compare the sets of damage parameters needed to model the strength and stiffness evolution of three types of rocks. Stress paths were the same as in the preceding analysis of crack opening and closure. It is shown that proper model calibration allows predicting the increase of temperature needed to propagate damage before mechanical compression, as compared to the temperature needed to propagate damage after cracks have already been produced by mechanical compression. It is also noted that the model can capture hardening and softening during thermo-mechanical closure (for damage parameters typical of sandstone). These numerical observations may guide the choice of rock material used in geotechnical design, especially for nuclear waste disposals or compressed air storage facilities. A proper understanding of the differences of behavior noted between the types of rock tested would require a multi-scale model, accounting for the various microscopic processes occurring at the grain scale. This will be the objective of a future work focused on rock healing and mechanical recovery.

Acknowledgments

The authors truly appreciate the most insightful comments and advice provided by Dr. M. Veveakis (CSIRO, Perth, Australia) to improve the section presenting thermodynamic modeling issues. During the discussions, the second author particularly enjoyed sharing journal articles, ideas and research vision about thermodynamics and geomechanics.

References

1. Abu Al-Rub R, Voyiadjis G (2003) On the coupling of anisotropic damage and plasticity models for ductile materials. Int J Solids Struct 40(11):2611–2643

2. Arson C, Gatmiri B (2010) Numerical study of a thermo-hydro-mechanical damage model for unsaturated porous media. Ann Solid Struct Mech 1(2):59–78
3. Arson C, Gatmiri B (2012) Thermo-hydro-mechanical modeling of damage in unsaturated porous media: Theoretical framework and numerical study of the edz. Int J Numer Anal Methods Geomech 36(3):272–306
4. Arson C, Xu H, Chester F (2012) On the definition of damage in time-dependent healing models for salt rock. Géotechnique Letters 2:67–71
5. Bésuelle P, Desrues J, Raynaud S (2000) Experimental characterisation of the localisation phenomenon inside a vosges sandstone in a triaxial cell. Int J Rock Mech Min Sci 37(8):1223–1237
6. de Borst R, Pamin J, Geers MG (1999) On coupled gradient-dependent plasticity and damage theories with a view to localization analysis. Eur J Mech Solids 18(6):939–962
7. Bryson L, Salehian A (2011) Performance of constitutive models in predicting behavior of remolded clay. Acta Geotech 6(3):143–154
8. Cauvin A, Testa R (1999) Damage mechanics: basic variables in continuum theories. Int J Solids Struct 36(5):747–761
9. Cekerevac C, Laloui L (2004) Experimental study of thermal effects on the mechanical behaviour of a clay. Int J Numer Anal Methods Geomech 28(3):209–228
10. Cervera M, Oliver J, Prato T (1999) Thermo-chemo-mechanical model for concrete. i: Hydration and aging. J Eng Mech 125(9):1018–1027
11. Chaboche JL (1992) Damage induced anisotropy: on the difficulties associated with the active/passive unilateral condition. Int J Damage Mech 1(2):148–171
12. Chaboche JL (1993) Development of continuum damage mechanics for elastic solids sustaining anisotropic and unilateral damage. Int J Damage Mech 2(4):311–329
13. Chaki S, Takarli M, Agbodjan W (2008) Influence of thermal damage on physical properties of a granite rock: Porosity, permeability and ultrasonic wave evolutions. Constr Build Mater 22(7):1456 – 1461
14. Chan K, Bodner S, Munson D (2001) Permeability of WIPP salt during damage evolution and healing. Int J Damage Mech 10(4):347–375
15. Chen Y, Zhou C, Jing L (2010) Numerical modeling of coupled thermo-mechanical response of a rock pillar. J Rock Mech Geotech Eng 2(3):262–273
16. Choo J, Kim Y, Lee J, Yun T, Lee J, Kim Y (2013) Stress-induced evolution of anisotropic thermal conductivity of dry granular materials. Acta Geotech 8:91–106
17. Collins I, Houlsby G (1997) Application of thermo-mechanical principles to the modelling of geotechnical materials. Proceedings of the Royal Society of London Series A: Mathematical, Physical and Engineering Sciences 453(1964):1975–2001
18. Cordebois J, Sidoroff F (1982) Endommagement anisotrope en élasticité et plasticité. J de Mécanique théorique et appliquée pp 45–60
19. Cowin S (1985) The relationship between the elasticity tensor and the fabric tensor. Mech Mater 4(2):137–147
20. David C, Menendez B, Darot M (1999) Influence of stress-induced and thermal cracking on physical properties and microstructure of la peyratte granite. Int J Rock Mech Min Sci 36(4):433 – 448
21. Desmorat R (2006) Positivité de la dissipation intrinsèque d'une classe de modèles d'endommagement anisotropes non standards. Comptes Rendus Mecanique 334(10):587–592
22. Dormieux L, Kondo D, Ulm FJ (2006) A micro mechanical analysis of damage propagation in fluid-saturated cracked media. CR Mécanique 334(7):440–446
23. Dragon A, Halm D, Désoyer T (2000) Anisotropic damage in quasi-brittle solids: modelling, computational issues and applications. Comput Methods Appl Mech Eng 183(3):331–352
24. Fortin J, Stanchits S, Vinciguerra S, Guéguen Y (2011) Influence of thermal and mechanical cracks on permeability and elastic wave velocities in a basalt from mt. etna volcano subjected to elevated pressure. Tectonophysics 503(1):60–74
25. Gawin D, Baggio P, Schrefler BA (1995) Coupled heat, water and gas flow in deformable porous media. International Journal for numerical methods in fluids 20(8-9):969–987
26. Giot R, Giraud A, Guillon T, Auvray C (2012) Three-dimensional poromechanical back analysis of the pulse test accounting for transverse isotropy. Acta Geotech 7(3):151–165
27. Grujovic N, Divac D, Zivkovic M, Slavkovic R, Milivojevic N, Milivojevic V, Rakic D (2013) An inelastic stress integration algorithm for a rock mass containing sets of discontinuities. Acta Geotech
28. Halm D, Dragon A (1998) An anisotropic model of damage and frictional sliding for brittle materials. Eur J Mech Solids 17(3):439–460
29. Halm D, Dragon A (2002) Modélisation de l'endommagement par mésofissuration du granite. Revue Francaise de Génie Civil 17:21–33
30. Heard H, Page L (1982) Elastic moduli, thermal expansion, and inferred permeability of two granites to 350 c and 55 megapascals. J Geophys Res: Solid Earth (1978–2012) 87(B11):9340–9348
31. Hejazi Y, Dias D, Kastner R (2008) Impact of constitutive models on the numerical analysis of underground constructions. Acta Geotech 3:251–258

32. Heuze F (1983) High-temperature mechanical, physical and thermal properties of granitic rocks—a review. Int J Rock Mech Min Sci Mech Abstr 20(1):3–10
33. Homand F, Chiarelli AS, Hoxha D (2002) Caractéristiques physiques et mécaniques du granite de la vienne et de l'argilite de l'est. Revue française de génie civil 6(1):11–20
34. Homand-Etienne F, Houpert R (1989) Thermally induced microcracking in granites: characterization and analysis. Int J Rock Mech Min Sci Mech Abstr 26(2):125–134
35. Hou Z (2003) Mechanical and hydraulic behavior of rock salt in the excavation disturbed zone around underground facilities. Int J Rock Mech Min Sci 40(5):725–738
36. Houlsby G, Puzrin A (2006) Principles of Hyperplasticity: An Approach to Plasticity Theory Based on Thermodynamic Principles. Springer
37. Hueckel T, Baldi G (1990) Thermoplasticity of saturated clays: experimental constitutive study. J Geotech Eng 116(12):1778–1796
38. Hueckel T, Borsetto M (1990) Thermoplasticity of saturated soils and shales: constitutive equations. Journal of Geotechnical Engineering 116(12):1765–1777
39. Hueckel T, Pellegrini R (2002) Reactive plasticity for clays: application to a natural analog of long-term geomechanical effects of nuclear waste disposal. Engineering geology 64(2):195–215
40. Hunsche U, Hampel A (1999) Rock salt — the mechanical properties of the host rock material rock salt - the mechanical properties of the host rock material for a radioactive waste repository. Eng Geol 52(3-4):271–291
41. Hütter M, Tervoort T (2008) Continuum damage mechanics: combining thermodynamics with a thoughtful characterization of the microstructure. Acta mechanica 201(1-4):297–312
42. Inada Y, Kinoshita N, Ebisawa A, Gomi S (1997) Strength and deformation characteristics of rocks after undergoing thermal hysteresis of high and low temperatures. Int J Rock Mech Min Sci 34(3–4):140.e1 – 140.e14
43. Jeong Hs, Kang Ss, Obara Y (2007) Influence of surrounding environments and strain rates on the strength of rocks subjected to uniaxial compression. Int J Rock Mech Min Sci 44(3):321–331
44. Jia Y, Wileveau Y, Su K, Duveau G, Shao JF (2007) Thermo-hydro-mechanical modelling of an in situ heating experiment. Géotechnique 57(10):845–855
45. Kachanov M (1992) Effective elastic properties of cracked solids: critical review of some basic concepts. Appl Mech Rev 45(8):304–335
46. Keller A, Hutter K (2011) On the thermodynamic consistency of the equivalence principle in continuum damage mechanics. Journal of the Mechanics and Physics of Solids 59(5):1115–1120
47. Keshavarz M, Pellet F, Loret B (2010) Damage and changes in mechanical properties of a gabbro thermally loaded up to 1,000 °c. Pure Appl Geophys 167(12):1511–1523
48. Konietzky H, Heftenberger A, Feige M (2009) Lifetime prediction for rocks under static compressive and tensile loads: a new simulation approach. Acta Geotech 4:73–78
49. Laloui L (2001) Thermo-mechanical behaviour of soils. Revue française de génie civil 5(6):809–843
50. Laloui L, Cekerevac C (2003) Thermo-plasticity of clays: An isotropic yield mechanism. Computers and Geotechnics 30(8):649–660
51. Lan H, Martin C, Andersson J (2013) Evolution of in situ rock mass damage induced by mechanical–thermal loading. Rock Mech Rock Eng 46(1):153–168
52. Lecampion B (2010) Stress-induced crystal preferred orientation in the poromechanics of inpore crystallization. J Mech Phys Solids 58:1701–1715
53. Lemaitre J, Desmorat R (2005) Engineering Damage Mechanics. Ductile, creep, fatigue and brittle failure. Springer - Verlag, Berlin Heidelberg
54. Levasseur S, Collin F, Charlier R, Kondo D (2011) A two-scale anisotropic damage model accounting for initial stresses in microcracked materials. Eng Fract Mech 78:1945–1956
55. Li L, Tang C, Wang S, Yu J (2013) A coupled thermo-hydrologic-mechanical damage model and associated application in a stability analysis on a rock pillar. Tunnelling Underground Space Tech 34:38–53
56. Liang WG, Xu SG, Zhao YS (2006) Experimental study of temperature effects on physical and mechanical characteristics of salt rock. Rock Mech Rock Eng 39(5):469–482
57. Lion M, Skoczylas F, Ledesert B (2005) Effects of heating on the hydraulic and poroelastic properties of bourgogne limestone. Int J Rock Mech Min Sci 42(4):508 – 520
58. Liu E, Xing H (2009) A double hardening thermo-mechanical constitutive model for overconsolidated clays. Acta Geotech 4(1):1–6
59. Liu J, Xie H, Hou Z, Yang C, Chen L (2013) Damage evolution of rock salt under cyclic loading in unixial tests. Acta Geotech
60. Liu R, Mao X, Zhang L, Ma D (2013) Thermal properties of mudstone at high temperature. Int J Geomech
61. Liu Z, Yu X (2011) Coupled thermo-hydro-mechanical model for porous materials under frost action: theory and implementation. Acta Geotech 6(2):51–65
62. Lu B, Torquato S (1992) Nearest-surface distribution functions for poly-dispersed particle systems. Phys Rev

A 45:5530–5544
63. Lubarda V, Krajcinovic D (1993) Damage tensors and the crack density distribution. Int J Solids Struct 30(20):2659–2677
64. Luong MP (1990) Tensile and shear strengths of concrete and rock. Eng Fract Mech 35(1-3):127–135
65. Mao XB, Zhang LY, Li TZ, Liu HS (2009) Properties of failure mode and thermal damage for limestone at high temperature. Min Sci Technol (China) 19(3):290–294
66. Mazars J, Berthaud Y, Ramtani S (1990) The unilateral behaviour of damaged concrete. Eng Fract Mech 35(4-5):629 – 635
67. McDermott CI, Randriamanjatosoa ARL, Tenzer H, Kolditz O (2006) Simulation of heat extraction from crystalline rocks: The influence of coupled processes on differential reservoir cooling. Geothermics 35(3):321–344
68. Nasseri M, Schubnel A, Benson P, Young R (2009) Common evolution of mechanical and transport properties in thermally cracked westerly granite at elevated hydrostatic pressure. Pure Appl Geophys 166(5-7):927–948
69. Oda M (1984) Similarity rules of crack geometry in statistically homogeneous rock masses. Mech Mater 3(2):119–129
70. Pecqueur G (1995) Étude expérimentale et modélisation du comportement d'une craie et d'un grès en torsion. PhD thesis, University of Lille I
71. Reuschle T, Haore SG, Darot M (2006) The effect of heating on the microstructural evolution of la peyratte granite deduced from acoustic velocity measurements. Earth and Planetary Science Letters 243(3–4):692 – 700
72. Rutqvist J, Freifeld B, Min KB, Elsworth D, Tsang Y (2008) Analysis of thermally induced changes in fractured rock permeability during 8 years of heating and cooling at the yucca mountain drift scale test. Int J Rock Mech Min Sci 45(8):1373–1389
73. Schrefler BA, Zhan X, Simoni L (1995) A coupled model for water flow, airflow and heat flow in deformable porous media. International Journal of Numerical Methods for Heat & Fluid Flow 5(6):531–547
74. Shao J, Zhou H, Chau K (2005) Coupling between anisotropic damage and permeability variation in brittle rocks. Int J Numer Anal Methods Geomech 29(12):1231–1247
75. Shi Y, Zhu Zd, Li Zj (2008) Deformation characteristics of deep-buried caverns considering thermal effect. Adv in Sci Technol Water Resour (China) 28(3):33–36
76. Stabler J, Baker G (2000) On the form of free energy and specific heat in coupled thermo-elasticity with isotropic damage. Int J Solids Struct 37(34):4691–4713
77. Sulem J, Ouffroukh H (2006) Shear banding in drained and undrained triaxial tests on a saturated sandstone: porosity and permeability evolution. Int J Rock Mech Min Sci 43(2):292–310
78. Swoboda G, Yang Q (1999) An energy-based damage model of geomaterials—i. formulation and numerical results. International journal of solids and structures 36(12):1719–1734
79. Tian H, Kempka T, Xu NX, Ziegler M (2012) Physical properties of sandstones after high temperature treatment. Rock Mech Rock Eng 45(6):1113–1117
80. Vorobiev O (2008) Generic strength model for dry jointed rock masses. Int J Plasticity 24(12):2221–2247
81. Voyiadjis GZ, Shojaei A, Li G (2011) A thermodynamic consistent damage and healing model for self healing materials. International Journal of Plasticity 27(7):1025–1044
82. Wawersik W, Hannum D (1980) Mechanical behavior of new mexico rock salt in triaxial compression up to 200 c. J Geophys Res: Solid Earth (1978–2012) 85(B2):891–900
83. Weinbrandt R, Casse F (1975) The effect of temperature on relative and absolute permeability of sandstones. Old SPE J 15(5):376–384
84. Wong TF (1982) Effects of temperature and pressure on failure and post-failure behavior of westerly granite. Mech Mater 1(1):3–17
85. Xianbiao M, Lianying Z, tianzhen L, haishun L (2009) Properties of failure mode and thermal damage for properties of failure mode and thermal damage for limestone at high temperature. Min Sci Technol (China) 19(3):0290–0294
86. Xu H, Arson C, Busetti S (2013) Modeling the anisotropic damaged zone around hydraulic fractures: Thermodynamic framework and simulation of mechanical tests. In: Proc. 47th US Rock Mech Geomech Symp, San Francisco, California, USA, pp Paper 13–375
87. Yavuz H, Demirdag S, Caran S (2010) Thermal effect on the physical properties of carbonate rocks. Int J Rock Mech Min Sci 47(1):94 – 103
88. Zhou H, Hu D, Zhang F, Shao J (2011) A thermoplastic/viscoplastic damage model for geomaterials. Acta Mechanica Solida Sinica 24(3):195 – 208
89. Zhu H, Yan Z, Deng T, Yao J, Zeng L, Qiang J (2006) Testing study on mechanical properties of tuff, granite and breccia after high temperatures. Chin J Rock Mech Eng 25(10):1